Classification of symmetry derived pairing at the *M* point in FeSe

P. Myles Eugenio* and Oskar Vafek
Florida State University and the National High Magnetic Field Lab, Tallahassee, Florida 32306, USA

(Received 27 April 2018; revised manuscript received 4 June 2018; published 6 July 2018)

Using the constraints imposed by the crystalline symmetry of FeSe and the experimentally observed phenomenology, we analyze the possible pairing symmetry of the superconducting order parameter focusing on intercalated and monolayer FeSe compounds. Such analysis leads to three possible pairing symmetry states—*s* wave, *d* wave, and helical *p* wave. Despite the differences in the pairing symmetry, each of these states is fully gapped with gap minimum centered above the normal state Fermi surface, in agreement with photoemission data of Zhang *et al.* [Phys. Rev. Lett. **117**, 117001 (2016)]. The analysis provides additional insights into the possible pairing mechanism for each of these states, highlighting the detrimental role of the renormalized repulsive intraorbital Hubbard U and interorbital U' and the beneficial role of the pair hopping J' and the Hund's J terms, as well as the spin-orbit coupling in the effective low-energy Hamiltonian.

DOI: 10.1103/PhysRevB.98.014503

I. INTRODUCTION

The wealth of physical phenomena exhibited by the iron-based superconductors has lead to an active field of research with challenging open questions [1,2]. Notable among them is the pairing symmetry and the mechanism of high temperature superconductivity which they exhibit [3,4]. Recently the focus has shifted towards the iron-selenide (FeSe) family of superconductors, with reported transition temperatures as high as 8 K in the bulk [5], 40 K in $(Li_{1-x}Fe_x)$OHFeSe [6], 65 K in monolayer FeSe grown on a $SrTiO_3$ [7], and even 109 K [8] in the latter system.

The monolayer FeSe is fundamentally a single iron plane with selenium atoms puckered in and out of that plane Fig. 1. In practice the 2D plane is grown on a substrate (e.g., $SrTiO_3$), leading to undoped [9] or doped [7,10,11] monolayer FeSe. Bulk FeSe [12–14] is a three dimensional crystal composed of vertically aligned FeSe planes. Additional three dimensional arrangements can be formed by sandwiching intercalates between the FeSe planes [6,15–17], where each stack is connected by a weak interlayer coupling [17].

The family of FeSe superconductors can thus be viewed as different arrangements of the *same material*, rather than altogether different materials. This suggests that the common structural unit, namely the FeSe plane, is responsible for the common electronic properties and, importantly, for superconductivity. Any differences in the physical characteristics—such as differences in T_c or the appearance of nematicity in the bulk FeSe, etc.—then presumably arise from differences in doping, strength of the interlayer coupling, inversion symmetry breaking of monolayer on a substrate, or from a nonelectronic origin (e.g., interface phonons) [10,11].

Indeed the common electronic feature to these materials is the presence of two electronlike Fermi surfaces centered at the Brillouin zone edge (the *M* point). Further, angularly resolved photoemission spectroscopy (ARPES) in the bulk [12,14], intercalated [16,17], and monolayer [7,10] shows that the electronlike Fermi surface bands originate from two separate binding energies at the *M* point (see Fig. 2). The bulk FeSe further exhibits a hole Fermi surface at the Brillouin zone center (Γ point) [12,14]; the intercalated and monolayer systems have only electron Fermi surfaces. These differences can be understood to be primarily due to the differences in the Fermi energy (doping), as opposed to changes in the band structure.

The superconducting gap in $(Li_{1-x}Fe_x)$OHFeSe is reported to be nodeless, nearly isotropic with gap size (13 ± 2) meV in Ref. [17], and ∼10 meV in Ref. [16]. Further, synchrotron ARPES in the monolayer shows an anisotropic gap, varying from 8 meV to 13 meV [7]. The superconducting gap is also claimed to show "back-bending," i.e., the gap sits directly above the normal state Fermi surfaces [7]. This last observation, upon which we elaborate later, is not trivial in that the separation between the two bands that cross the Fermi surface in the ΓM direction is only about ∼15 meV (see Fig. 2 in Ref. [7]), thus comparable to the pairing gap itself.

Scanning tunneling microscopy (STM) experiments also support the existence of a large superconducting gap in these materials [6,18]. More interestingly, they show a hard gap followed by not one but *two* peaks in the dI/dV, Fig. 3 [6]. The two peaks occur at 8.6 meV and 14.3 meV in intercalated $(Li_{1-x}Fe_x)$OHFeSe [6] and 9 meV and 20.1 meV in monolayer [18]. The suggestion that the higher energy peak directly reflects the superconducting gap is at odds with the monolayer ARPES data, whose gap maximum is, as we stated, ∼13 meV (as shown in Fig. 4 of Ref. [7], it never exceeds 14 meV, even considering experimental uncertainty).

In this paper, we concentrate on understanding to what degree do the crystalline symmetry of FeSe, and the experimentally observed phenomenology mentioned above, constrain the possible pairing symmetry of the superconducting order parameter. We focus on intercalated $(Li_{1-x}Fe_x)$OHFeSe and monolayer FeSe epitaxially grown on $SrTiO_3$ where the 3D dispersion effects are absent (although we ignore the inversion symmetry breaking due to the substrate in the monolayer FeSe). To this end, we build upon the low energy model that

*eugenio.myles@gmail.com

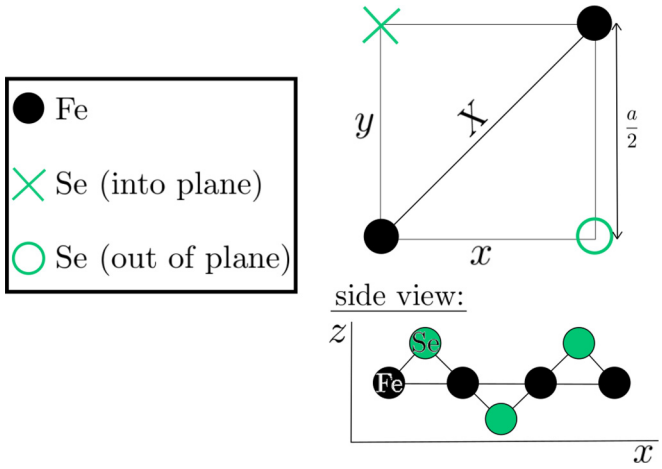

FIG. 1. Unit cell of the FeSe plane. There are 2-Fe per unit cell, with Se atoms puckered above and below the Fe plane. The constant a is the lattice spacing. The space group of the iron selenide is discussed in Ref. [19]. The three space group generators [19] are a mirror across the yz plane m_x, a mirror across the Yz plane m_X followed by a $(\frac{a}{2},\frac{a}{2})$ translation, and an xy-plane mirror m_z followed by a $(\frac{a}{2},\frac{a}{2})$ translation, where $X = x + y$ and $Y = -x + y$.

respects the full space group symmetry of the material and includes spin-orbit effects [19], but extend it in ways that better account for the observed phenomenology of FeSe. Such analysis leads us to three possible pairing symmetry states—s wave, d wave, and helical p wave. Despite the differences in the pairing symmetry, each of these states is fully gapped with gap minimum centered above the normal state Fermi surface. Our analysis also gives us insight into the possible pairing mechanism for each of these states, highlighting the detrimental role of the repulsive intraorbital Hubbard U and interorbital U', and the beneficial role of the pair hopping J' and

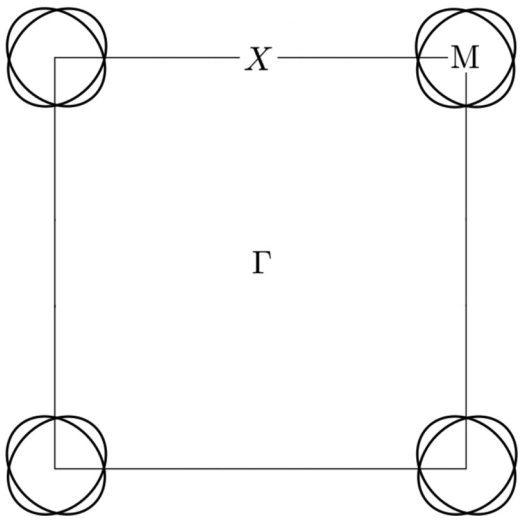

FIG. 2. Sketch of Fermi surfaces as seen in intercalated and monolayer FeSe. There are two points of high symmetry: the Brillouin zone center $\Gamma = (0,0)$ and the zone edge $M = (\frac{\pi}{a},\frac{\pi}{a})$. In the proper 2-Fe/UC picture (shown here), two electron pockets cross at the M point. The Fermi surface crossing occurs along the MX direction, where X marks the Brillouin zone boundary.

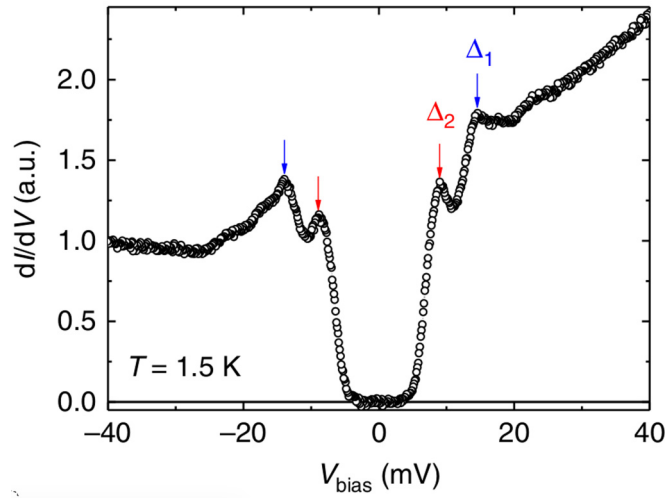

FIG. 3. Experimental result Fig. (2.C), taken from Ref. [6] under the Creative Commons Attribution 4.0 International License.

the Hund's J terms in the effective low-energy Hamiltonian. (As explained in Sec. II B each of the interaction couplings should be understood as renormalized and orbital or, more precisely, Bloch function dependent.) The Hund's coupling, together with spin orbit coupling, was recently proposed by one of us and Chubukov to explain the phenomenology and the mechanism of pairing in KFe_2As_2 [20]. This is another example of an iron-based superconductor with only one carrier type (hole) Fermi surface.

The paper is organized as follows. In Sec. II, we introduce the low energy effective model—including a new momentum-dependent *intrapocket* spin-orbit coupling—as well as the symmetry allowed interaction couplings. In Sec. III, we determine the values of the symmetry allowed parameters in the normal state based on the detailed comparison with the ARPES experiment. In Sec. IV we classify all pairing states based on the symmetry. Armed with the values of the parameters obtained in Sec. III, we then highlight the details of the phenomenology of the superconducting state, and critically compare them with the predictions for all pairing states. Assuming an overall time

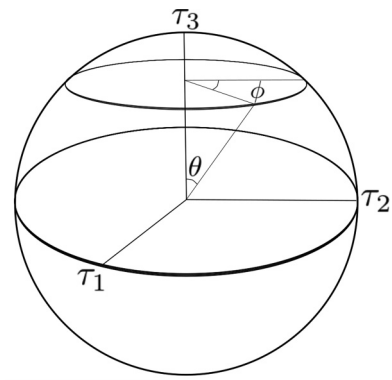

FIG. 4. Bloch sphere. The unit sphere embedded in a 3D space, where each orthogonal direction is associated with an SU(2) generator. The north pole ($+\tau_3$ direction) and south pole ($-\tau_3$ direction) represent the $M1$ and $M3$ reference states, respectively.

reversal symmetry, we find that only s, d, and helical p states are compatible with the mentioned phenomenology. Section V provides detailed analysis of the three pairing states. The discussion and the outlook are presented in the final section.

II. MODEL

We employ an itinerant model developed in Ref. [19] for the electronlike Fermi surfaces at the M point. This low energy effective theory is constructed by requiring invariance under the FeSe space group symmetries and time reversal. Using the nomenclature of Ref. [19], the two electronically relevant M-point representations are $M1$ and $M3$. We construct doublets $\psi_{X,\alpha}(\mathbf{k}) = (1_{X,\alpha}(\mathbf{k}), 3_{X,\alpha}(\mathbf{k}))^T$ and $\psi_{Y,\alpha}(\mathbf{k}) = (1_{Y,\alpha}(\mathbf{k}), 3_{Y,\alpha}(\mathbf{k}))^T$. Our starting Hamiltonian in the normal state is

$$H_0 = \sum_{\mathbf{k}} \sum_{\alpha\beta=\uparrow,\downarrow} \psi^\dagger_{M,\alpha}(\mathbf{k}) \begin{pmatrix} h'^{\alpha\beta}_X(\mathbf{k}) & \Lambda_{\alpha\beta} \\ \Lambda^\dagger_{\alpha\beta} & h'^{\alpha\beta}_Y(\mathbf{k}) \end{pmatrix} \psi_{M,\beta}(\mathbf{k}), \quad (1)$$

where

$$\psi_{M,\alpha}(\mathbf{k}) = (\psi_{X,\alpha}(\mathbf{k}), \psi_{Y,\alpha}(\mathbf{k}))^T. \quad (2)$$

The matrix h'_X in Eq. (1) is the Hamiltonian for one electronlike pocket:

$$\begin{aligned} h'^{\alpha\beta}_X(\mathbf{k}) &= h_X(\mathbf{k})\delta^{\alpha\beta} \\ &\quad + [\lambda_z(k_x - k_y) + p_{z1}(k_x^3 - k_y^3) \\ &\quad + p_{z2}k_xk_y(-k_x + k_y)]\sigma_3^{\alpha\beta}\tau_1, \end{aligned} \quad (3)$$

where τ_i and σ_i are Pauli matrices acting in orbital and spin space, respectively. This is an extension of the Hamiltonian for a single electron pocket h_X, developed in Ref. [19]:

$$\begin{aligned} h_X(\mathbf{k}) &= \begin{pmatrix} \epsilon_1 + \frac{k^2}{2m_1} + a_1k_xk_y & -iv(k_x + k_y) \\ iv(k_x + k_y) & \epsilon_3 + \frac{k^2}{2m_3} + a_3k_xk_y \end{pmatrix} \\ &\equiv h_{X0}(\mathbf{k}) + h_{X3}(\mathbf{k})\tau_3 + h_{X2}(\mathbf{k})\tau_2. \end{aligned} \quad (4)$$

Because the Hamiltonian $h'^{\alpha\beta}_X(\mathbf{k})$ is diagonal in spin space, its spin-diagonal elements will be referred to as $h'^{\uparrow}_X \equiv h'^{\uparrow\uparrow}_X$ and $h'^{\downarrow}_X \equiv h'^{\downarrow\downarrow}_X$.

The motivation for extending the Hamiltonian is explained in Sec. III. The prefactor of the k-linear term is denoted λ_z, because it couples the orbital degrees of freedom with the out-of-plane spin σ_z; k-cubic terms were also introduced with prefactors p_{z1} and p_{z2}. It should be noted that this momentum-dependent spin-orbit acts *within* each pocket and does not mix the electron pockets, i.e., it is intraband. The extended Hamiltonian for the second electron pocket at the M point can again be obtained by performing a mirror reflection in the yz plane:

$$h'_Y(k_x, k_y) = \frac{\sigma_1 - \sigma_2}{\sqrt{2}} h'_X(-k_x, k_y) \frac{\sigma_1 - \sigma_2}{\sqrt{2}}. \quad (5)$$

Note that $\sigma_3\tau_1$ changed sign under the mirror reflection, because σ_3 is an axial vector.

It was further shown in Ref. [19] that a momentum-independent interband spin-orbit coupling is allowed by symmetry. Such term, parametrized by λ, comes from the coupling of the orbital degrees of freedom with the in-plane spin vector $\vec{\sigma} = (\sigma_X, \sigma_Y)$, thus breaking the spin SU(2) symmetry:

$$\begin{aligned} h_{\mathrm{SOC}} &= \sum_{\mathbf{k}} \sum_{\alpha\beta=\uparrow,\downarrow} \psi^\dagger_{X,\alpha}\Lambda_{\alpha\beta}\psi_{Y,\beta} + \mathrm{H.c.} \\ &= \sum_{\mathbf{k}} \psi^\dagger_{X,\uparrow} \begin{pmatrix} 0 & i\lambda \\ \lambda & 0 \end{pmatrix} \psi_{Y,\downarrow} + \psi^\dagger_{X,\downarrow} \begin{pmatrix} 0 & i\lambda \\ -\lambda & 0 \end{pmatrix} \psi_{Y,\uparrow} \\ &\quad + \mathrm{H.c.} \end{aligned} \quad (6)$$

Another important consequence of this (interband) h_{SOC} is the lifting of the degeneracy in the direction of the Fermi surface crossing, leading to the formation of an "inner" and "outer" Fermi surface (see Fig. 5).

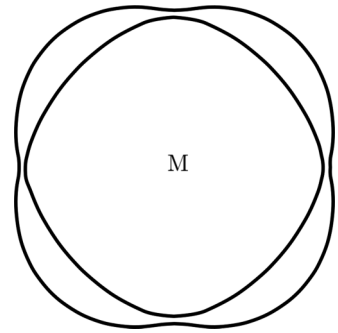

FIG. 5. Sketch of electron pockets at the M point in the presence of an interband spin-orbit coupling λ. The band degeneracy in the MX direction is lifted, and the Fermi surface crossing becomes avoided. Two new Fermi surfaces are formed—an inner and outer pocket.

A. Bloch sphere

The Hamiltonian for an electron pocket h'_X has one band that disperses downward and one band that disperses upward and crosses the Fermi level. Because the difference in energy between the bands at the Fermi level and the bands below the Fermi level is an order of magnitude larger than the pairing scale, it is useful to project onto the prior. This reduces the size of the Hamiltonian by half, facilitating the symmetry analysis.

This projected basis can be visualized in terms of a Bloch sphere, Fig. 4. For each spin-diagonal element, we write the nonidentity part of Eq. (3) as

$$\begin{aligned} \not{h} &\equiv h'^{\uparrow}_X(\mathbf{k}) - h_{X0}(\mathbf{k}) \\ &= h_{X3}(\mathbf{k})\tau_3 + h_{X2}(\mathbf{k})\tau_2 + h_{X1}(\mathbf{k})\tau_1, \end{aligned} \quad (7)$$

noting that $\not{h}$ and $h'^{\uparrow}_X$ have equivalent eigenstates. We can then define

$$\hat{\not{h}} \equiv \frac{\not{h}}{|\not{h}|} = \begin{pmatrix} \cos\theta & \sin\theta\, e^{-i\phi} \\ \sin\theta\, e^{i\phi} & -\cos\theta \end{pmatrix}, \quad (8)$$

where the Bloch angles are functions of momentum $(\theta(\mathbf{k}), \phi(\mathbf{k}))$. The up- and down-spin Hamiltonians map into each other as $h'^{\uparrow}_X(\theta, \pi - \phi) = h'^{\downarrow}_X(\theta, \phi)$, and the two elec-

tron pockets map into each other as $h'^{\uparrow}_X(\theta(-k_x,k_y),\pi-\phi(-k_x,k_y)) = h'^{\uparrow}_Y(\theta(k_x,k_y),\phi(k_x,k_y))$.

The eigenstate of $h'^{\uparrow}_X$ that crosses the Fermi level has the form

$$|X\uparrow\rangle = \left(\cos\frac{\theta}{2}\, e^{-i\phi}, \sin\frac{\theta}{2}\right)^T. \tag{9}$$

All other eigenstates can be obtained through the above mentioned symmetry relationships.

B. Interactions

There are 14 SU(2) invariant couplings at the M point which contribute to the interacting Hamiltonian $H^{\mathrm{M}}_{\mathrm{int}}$. We write each interaction in terms of the $M1$ and $M3$ symmetry representations, using the doublets $1_\alpha = (1_{X,\alpha}, 1_{Y,\alpha})^T$ and $3_\alpha = (3_{X,\alpha}, 3_{Y,\alpha})^T$. The 14 couplings are listed in Eq. (10) in a form facilitating to applying mean field, and with each coupling constant being labeled by the symmetry of the corresponding mean field order parameter listed in Tables III, IV, and V:

$$\begin{aligned}
H^{\mathrm{M}}_{\mathrm{int}} = \sum_{\mathbf{k}} \sum_{\alpha,\beta\in\{\uparrow,\downarrow\}} & g^{(1)}_{A_{1g}} 1^\dagger_\alpha(\mathbf{k})\tau_0 1^*_\beta(-\mathbf{k}) 1^T_\beta(-\mathbf{k})\tau_0 1_\alpha(\mathbf{k}) + g^{(1)}_{B_{2g}} 1^\dagger_\alpha(\mathbf{k})\tau_3 1^*_\beta(-\mathbf{k}) 1^T_\beta(-\mathbf{k})\tau_3 1_\alpha(\mathbf{k}) \\
& + g^{(1)}_{A_{2u}} 1^\dagger_\alpha(\mathbf{k})\tau_1 1^*_\beta(-\mathbf{k}) 1^T_\beta(-\mathbf{k})\tau_1 1_\alpha(\mathbf{k}) + g^{(1)}_{B_{1u}} 1^\dagger_\alpha(\mathbf{k})\tau_2 1^*_\beta(-\mathbf{k}) 1^T_\beta(-\mathbf{k})\tau_2 1_\alpha(\mathbf{k}) + g^{(3)}_{A_{1g}} 3^\dagger_\alpha(\mathbf{k})\tau_0 3^*_\beta(-\mathbf{k}) 3^T_\beta(-\mathbf{k})\tau_0 3_\alpha(\mathbf{k}) \\
& + g^{(3)}_{B_{2g}} 3^\dagger_\alpha(\mathbf{k})\tau_3 3^*_\beta(-\mathbf{k}) 3^T_\beta(-\mathbf{k})\tau_3 3_\alpha(\mathbf{k}) + g^{(3)}_{B_{2u}} 3^\dagger_\alpha(\mathbf{k})\tau_1 3^*_\beta(-\mathbf{k}) 3^T_\beta(-\mathbf{k})\tau_1 3_\alpha(\mathbf{k}) + g^{(3)}_{A_{1u}} 3^\dagger_\alpha(\mathbf{k})\tau_2 3^*_\beta(-\mathbf{k}) 3^T_\beta(-\mathbf{k})\tau_2 3_\alpha(\mathbf{k}) \\
& + g^{t}_{E_u}((1^\dagger_\alpha(\mathbf{k})\tau_0(\sigma_2\sigma_j)_{\alpha\beta} 3^*_\beta(-\mathbf{k}))(3^T_\mu(-\mathbf{k})\tau_0(\sigma_j\sigma_2)_{\mu\nu} 1_\nu(\mathbf{k})) + (1^\dagger_\alpha(\mathbf{k})\tau_3(\sigma_2\sigma_j)_{\alpha\beta} 3^*_\beta(-\mathbf{k}))(3^T_\mu(-\mathbf{k})\tau_3(\sigma_j\sigma_2)_{\mu\nu} 1_\nu(\mathbf{k}))) \\
& + g^{s}_{E_u}((1^\dagger_\alpha(\mathbf{k})\tau_0(\sigma_2)_{\alpha\beta} 3^*_\beta(-\mathbf{k}))(3^T_\mu(-\mathbf{k})\tau_0(\sigma_2)_{\mu\nu} 1_\nu(\mathbf{k})) + (1^\dagger_\alpha(\mathbf{k})\tau_3(\sigma_2)_{\alpha\beta} 3^*_\beta(-\mathbf{k}))(3^T_\mu(-\mathbf{k})\tau_3(\sigma_2)_{\mu\nu} 1_\nu(\mathbf{k}))) \\
& + g^{t}_{E_g}((1^\dagger_\alpha(\mathbf{k})\tau_1(\sigma_2\sigma_j)_{\alpha\beta} 3^*_\beta(-\mathbf{k}))(3^T_\mu(-\mathbf{k})\tau_1(\sigma_j\sigma_2)_{\mu\nu} 1_\nu(\mathbf{k})) + (1^\dagger_\alpha(\mathbf{k})\tau_2(\sigma_2\sigma_j)_{\alpha\beta} 3^*_\beta(-\mathbf{k}))(3^T_\mu(-\mathbf{k})\tau_2(\sigma_j\sigma_2)_{\mu\nu} 1_\nu(\mathbf{k}))) \\
& + g^{s}_{E_g}((1^\dagger_\alpha(\mathbf{k})\tau_1(\sigma_2)_{\alpha\beta} 3^*_\beta(-\mathbf{k}))(3^T_\mu(-\mathbf{k})\tau_1(\sigma_2)_{\mu\nu} 1_\nu(\mathbf{k})) + (1^\dagger_\alpha(\mathbf{k})\tau_2(\sigma_2)_{\alpha\beta} 3^*_\beta(-\mathbf{k}))(3^T_\mu(-\mathbf{k})\tau_2(\sigma_2)_{\mu\nu} 1_\nu(\mathbf{k}))) \\
& + g^{(13)}_{A_{1g}}(1^\dagger_\alpha(\mathbf{k})\tau_0 1^*_\beta(-\mathbf{k}) 3^T_\beta(-\mathbf{k})\tau_0 3_\alpha(\mathbf{k}) + 3^\dagger_\alpha(\mathbf{k})\tau_0 3^*_\beta(-\mathbf{k}) 1^T_\beta(-\mathbf{k})\tau_0 1_\alpha(\mathbf{k})) \\
& + g^{(13)}_{B_{2g}}(1^\dagger_\alpha(\mathbf{k})\tau_3 1^*_\beta(-\mathbf{k}) 3^T_\beta(-\mathbf{k})\tau_3 3_\alpha(\mathbf{k}) + 3^\dagger_\alpha(\mathbf{k})\tau_3 3^*_\beta(-\mathbf{k}) 1^T_\beta(-\mathbf{k})\tau_3 1_\alpha(\mathbf{k})).
\end{aligned} \tag{10}$$

These 14 invariant couplings can be given a physical meaning by relating them to the "Bloch" Kanamori couplings U_a, U'_a, J_a, and J'_a, where the couplings are split into couplings which are symmetry related. The on-site Bloch-Kanamori Hamiltonian is Eq. (11), which takes into account the iron mirror symmetries:

$$\begin{aligned}
& H_{\mathrm{BK}}(\mathbf{R}\equiv\mathbf{R_i}+\boldsymbol{\delta}) \\
& = \frac{1}{2}\sum_m U_m \sum_{\alpha\beta} d^\dagger_{m\alpha}(\mathbf{R}) d_{m\alpha}(\mathbf{R}) d^\dagger_{m\beta}(\mathbf{R}) d_{m\beta}(\mathbf{R}) \\
& + \frac{1}{2}\sum_{m\neq m'} U'_{mm'} \sum_{\alpha\beta} d^\dagger_{m\alpha}(\mathbf{R}) d_{m\alpha}(\mathbf{R}) d^\dagger_{m'\beta}(\mathbf{R}) d_{m'\beta}(\mathbf{R}) \\
& + \frac{1}{2}\sum_{m\neq m'} J_{mm'} \sum_{\alpha\beta} d^\dagger_{m\alpha}(\mathbf{R}) d_{m'\alpha}(\mathbf{R}) d^\dagger_{m'\beta}(\mathbf{R}) d_{m\beta}(\mathbf{R}) \\
& + \frac{1}{2}\sum_{m\neq m'} J'_{mm'} \sum_{\alpha\beta} d^\dagger_{m\alpha}(\mathbf{R}) d_{m'\alpha}(\mathbf{R}) d^\dagger_{m\beta}(\mathbf{R}) d_{m'\beta}(\mathbf{R}).
\end{aligned} \tag{11}$$

Using the method discussed in Ref. [19], we relate the parameters of the symmetry allowed couplings of Eq. (10) to Bloch-Kanamori couplings of Eq. (11). The results are listed in Table I, and again with their corresponding mean field order parameters in Tables III, IV, and V.

Lastly, it should be noted that we consider only tree-level electron-electron Coulomb-type interactions, owing to the existence of electronlike (and no holelike) Fermi surfaces in monolayer [7] and intercalated FeSe [16,17]. In literature it has been shown that attractive interactions can be produced in monolayer FeSe by coupling to nematic-orbital [21] and spin [22] fluctuations, which lead to spin-singlet s- and d-wave superconductivity, respectively. However, this analysis highlights an important problem for these mechanisms: any attractive interaction in the spin-singlet s-wave (A_{1g}) and d-wave (B_{2g}) channels must overcome the large intraorbital Hubbard repulsion U_a in order to stabilize pairing.

TABLE I. Invariant coupling constants.

$g^{(1)}_{A_{1g}}$	$U_1 + J'_{11}$
$g^{(1)}_{B_{2g}}$	$U_1 - J'_{11}$
$g^{(1)}_{A_{2u}}$	$U'_1 + J_{11}$
$g^{(1)}_{B_{1u}}$	$U'_1 - J_{11}$
$g^{(3)}_{A_{1g}}$	$U_3 + J'_{33}$
$g^{(3)}_{B_{2g}}$	$U_3 - J'_{33}$
$g^{(3)}_{B_{2u}}$	$U'_3 + J_{33}$
$g^{(3)}_{A_{1u}}$	$U'_3 - J_{33}$
$g^{t}_{E_u}$	$U'_{1X3X} - J_{1X3X}$
$g^{s}_{E_u}$	$U'_{1X3X} + J_{1X3X}$
$g^{t}_{E_g}$	$U'_{1X3Y} - J_{1X3Y}$
$g^{s}_{E_g}$	$U'_{1X3Y} + J_{1X3Y}$
$g^{(13)}_{A_{1g}}$	$J'_{1X3X} + J'_{1X3Y}$
$g^{(13)}_{B_{2g}}$	$J'_{1X3X} - J'_{1X3Y}$

TABLE II. Luttinger invariants: FeSe. These parameters were acquired by fitting Eq. (4) to bulk ARPES data [12].

a_1	782.512 meV Å^2
a_3	−1400 meV Å^2
$\frac{1}{2m_1}$	−492.01 meV Å^2
$\frac{1}{2m_3}$	1494.14 meV Å^2
v	224.406 meV Å

III. MODEL-EXPERIMENT COMPARISON AND FITS

In Sec. II we discussed the low-energy effective theory derived from the FeSe plane's space group symmetry. The low-energy theory captures four electronically relevant bands emerging from two 2D symmetry representations at the M point, $M1$ and $M3$. The energy of these representations at the M point are ϵ_1 and ϵ_3; the precise geometry of these bands emerging away from the M point depends on values of the Luttinger invariants: a_1, a_3, m_1, m_3, and v. We constrain our model by fitting the invariants to bulk FeSe ARPES [12], which clearly displays bands originating at the M point at $\epsilon_1 = -5$ meV and $\epsilon_3 = -55$ meV. Because of the shared structural unit (the FeSe plane), the intercalated and monolayer FeSe systems should have the same Luttinger invariants as Table II, up to a uniform shift in the binding energies ϵ_1 and ϵ_3 by ~ -50 meV.

The presence of interband spin-orbit coupling has been shown in other Fe-based superconductors [23], the effect of which is a splitting of the band degeneracy in the direction of the Fermi surface crossing (XM direction) and an avoidance of the Fermi surface crossing (see Fig. 5). The monolayer FeSe shows a band structure comprised of two electronlike Fermi surfaces at the M point with no mixing of the Fermi surfaces up to an $\sim$5 meV resolution [7]. This constraint on the size of the interband spin-orbit coupling λ, which directly leads to the Fermi surface avoidance, is further supported by photoemission in bulk FeSe, which shows no resolved avoided crossing [12,13]. However, ARPES in the bulk [13] further shows an 11 meV band splitting below the Fermi level in the ΓM direction. This band splitting cannot be described by an interband spin-orbit coupling, which opens a splitting of order λ in the direction of the crossing, yet only opens a splitting of order $\lambda^2/|\epsilon_1 - \epsilon_3|$ in the ΓM direction below the Fermi level. Simply put, an interband spin-orbit coupling large enough to open the 11 meV splitting below the Fermi level would violate experiment by producing a large Fermi surface avoidance.

In order to resolve this problem, we introduced the symmetry allowed k-linear intraband spin-orbit coupling λ_z [and higher order invariants p_{z1} and p_{z2}; see Eq. (3)]. This term directly splits the band crossing below the Fermi level but does not mix the two bands that cross the Fermi level, thus supporting an 11 meV splitting (shown in the ΓM direction in Fig. 6), while not avoiding the electron Fermi surfaces.

In classifying and disqualifying pairing states, it is practical to constrain the many parameters of the model; however, limiting the study to an overconstrained model risks unjustifiably disqualifying states. Thus we constrain the Luttinger invariants of our model to Table II, as discussed above, and allow for the values of the bands at the M point to vary in a ± 10 meV window about $\epsilon_1 = -55$ meV and $\epsilon_3 = -105$ meV (for intercalated and monolayer FeSe). With respect to the spin-orbit couplings, we choose λ_z (and higher order invariants) so as to produce a splitting less than or equal to 20 meV below the Fermi level, and we constrain interband spin-orbit $\lambda \leqslant 5$ meV as discussed previously. These constraints are chosen with the understanding that the key features to reproduce in the normal state are two bands crossing the Fermi level to produce two electronlike Fermi surfaces, and where superconductivity primarily depends on the band structure close to the Fermi level.

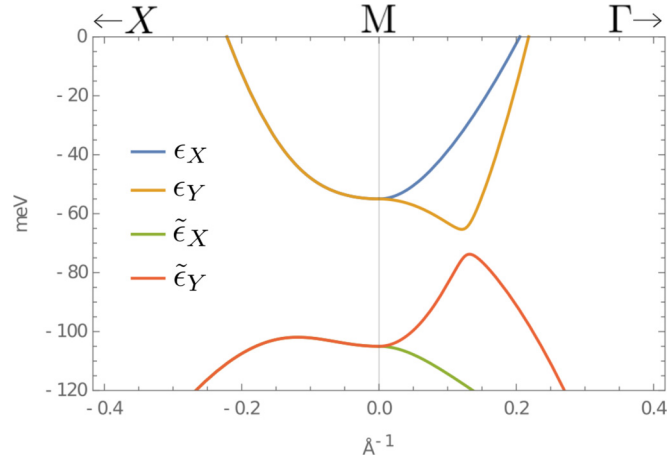

FIG. 6. Band structure in the ΓM and XM directions. The interband spin-orbit coupling is turned off ($\lambda = 0$) thus the bands are fourfold degenerate in the XM direction. It should be noted that, away from high symmetry directions, each band has a double degeneracy, due to inversion and time-reversal symmetry. The other model parameters used here are the Luttinger invariants Table II from fitting Ref. [12], and the following: $\lambda_z = 26$ meV Å^{-1}, $p_{z1} = p_{z2} = 0$, $\epsilon_1 = -55$ meV, and $\epsilon_3 = -105$ meV. The bands ϵ_X and $\tilde{\epsilon}_X$ are the eigenstates of $h_X^{'\alpha}$ [see Eq. (3) and below Eq. (4)]; the bands ϵ_Y and $\tilde{\epsilon}_Y$ are the eigenstates of $h_Y^{'\alpha}$, where $\alpha = \uparrow$ or $\downarrow$.

IV. PAIRING AND SPIN-ORBIT COUPLING

In the absence of any spin-orbit coupling, the Hamiltonian has full SU(2) spin symmetry. The intraband spin-orbit λ_z couples the orbital degrees of freedom to the out-of-plane spin, reducing the SU(2) spin symmetry to U(1). This reduced U(1) symmetry reflects the freedom to rotate the in-plane spin vector $\vec{\sigma} = (\sigma_1, \sigma_2)$ about the z axis.

In simpler terms, space group operations act on the orbital degrees of freedom (τ_i), while the spin transformations act on the spin degrees of freedom (σ_i). The introduction of a term in the Hamiltonian that goes as some product of τ_i and σ_i demands that space group and spin transformations transform *together* so as to preserve the invariance of the Hamiltonian under space group transformations. The out-of-plane spin-orbit λ_z introduces a term in the Hamiltonian that is proportional to σ_z. Thus, while rotations about the z axis are still symmetries of the Hamiltonian, i.e., $[\sigma_z, H] = 0$, rotations about any in-plane spin axis must be accompanied by rotations in the orbital space.

Only the spin-triplet pairing terms, whose generic form is

$$\vec{d} \cdot \psi^T_{M,\alpha}(-\mathbf{k})(i\sigma_2\vec{\sigma})^{\alpha\beta}\psi_{M,\beta}(\mathbf{k}),$$

are effected by spin-orbit coupling. Without spin-orbit coupling, spin triplets have a full SU(2) spin symmetry and thus the freedom to rotate the $\vec{d}$ vector in any direction. The introduction of λ_z decouples the out-of-plane component of $\vec{d}$ from its in-plane component. Triplets formed from in-plane $\vec{d}$ vector, i.e., $i\sigma_2\vec{\sigma} = i\sigma_2(\sigma_1,\sigma_2)$, have their spin symmetry reduced to U(1) and are free to rotate about the z axis. On the other hand, the out-of-plane spin-triplet pairs, with $\vec{d}$ vector $i\sigma_2\sigma_3$, become fixed and transform identically to (i.e., same irreducible representation as) a singlet pair.

Before breaking the remaining U(1) spin symmetry, the in-plane spin mirror (which is written in terms of Pauli matrices in spin space as $i\sigma_z$) is a symmetry of the Hamiltonian; thus the orbital and spin degrees of freedom are not constrained to transform together under the in-plane mirror m_z. In this scenario spinors ψ_X and ψ_Y transform odd and even under the in-plane mirror, respectively, independent of their spin index. Thus intraband pairings of the form $\psi_X \otimes \psi_X$ and $\psi_Y \otimes \psi_Y$ transform even under the in-plane mirror, while interband pairings of the form $\psi_X \otimes \psi_Y$ transform odd under the in-plane mirror.

Introducing momentum independent spin-orbit λ breaks the remaining spin symmetry. This means that now $[\sigma_z, H] \neq 0$ and thus there exists no axis of rotation in spin space about which the Hamiltonian is invariant. The spinors ψ_X^α and ψ_Y^α are now required to transform both orbital and spin together under the in-plane mirror. Consequently, now intraband pairings with opposite-spin $\psi_X^\uparrow \otimes \psi_X^\downarrow$ and interband pairings with same-spin $\psi_X^\uparrow \otimes \psi_Y^\uparrow$ transform even under the in-plane mirror, while intraband pairings with like-spin $\psi_X^\uparrow \otimes \psi_X^\uparrow$ and interband pairings with opposite-spin $\psi_X^\uparrow \otimes \psi_Y^\downarrow$ transform odd.

This in turn divides pairing into two classes: those pairings even under the in-plane mirror, Table IV, and those which are odd, Table V. The even class is represented by the Ψ_1 Nambu spinor,

$$\Psi_1(\mathbf{k}) = (\psi_X^\uparrow(\mathbf{k}), \psi_Y^\downarrow(\mathbf{k}), \psi_X^{\downarrow\dagger}(-\mathbf{k}), -\psi_Y^{\uparrow\dagger}(-\mathbf{k}))^T. \quad (12)$$

The odd class is represented by Ψ_{2a} and Ψ_{2b},

$$\begin{aligned}\Psi_{2a}(\mathbf{k}) &= (\psi_X^\uparrow(\mathbf{k}), \psi_Y^\downarrow(\mathbf{k}), \psi_X^{\uparrow\dagger}(-\mathbf{k}), -\psi_Y^{\downarrow\dagger}(-\mathbf{k}))^T,\\ \Psi_{2b}(\mathbf{k}) &= (\psi_X^\downarrow(\mathbf{k}), \psi_Y^\uparrow(\mathbf{k}), \psi_X^{\downarrow\dagger}(-\mathbf{k}), -\psi_Y^{\uparrow\dagger}(-\mathbf{k}))^T.\end{aligned} \quad (13)$$

The two classes are completely independent, with no single irreducible (pairing) representation of the symmetry existing in both classes simultaneously.

The two spinors in the odd classes Ψ_{2a} and Ψ_{2b} are related by a spin flip. They constitute Kramer's pairs, which are independent in the presence of inversion symmetry. This is evident in the double degeneracy of the bands throughout the Brillouin zone. As a consequence of spin-orbit coupling, Ψ_{2a} and Ψ_{2b} map into one another under the 45° mirror m_X. This mapping of independent spinors into one another allows for odd class pairing states to change sign under the mirror m_X without requiring a node.

Comparison to experiment

The absence of a Fermi surface avoidance (to within ~ 5 meV experimental resolution) in the monolayer FeSe [7] seems to suggest that interband spin-orbit coupling λ does not play the primary role in superconductivity at the M point, although, as we discuss later, it does play a secondary role. In Table III we list all symmetry derived pairing states at the M point in absence of interband spin-orbit coupling λ. They are separated into two symmetry separated classes—intraband and interband pairing. To understand this distinction, note that the energies of the single-particle fermionic excitations are the positive eigenvalues of the matrix

$$\begin{pmatrix} \epsilon_X(\mathbf{k}) & 0 & \Delta_X^* & \Delta_{YX}^* \\ 0 & \epsilon_Y(\mathbf{k}) & \Delta_{XY}^* & \Delta_Y^* \\ \Delta_X & \Delta_{XY} & -\epsilon_X(\mathbf{k}) & 0 \\ \Delta_{YX} & \Delta_Y & 0 & -\epsilon_Y(\mathbf{k}) \end{pmatrix}.$$

The $\epsilon_X(\mathbf{k})$ is the normal state band energy of the pocket X [i.e., eigenvalue of Eq. (3)], and similarly $\epsilon_Y(\mathbf{k})$ is the band energy of the pocket Y. The intraband Δ_X and Δ_Y pair directly on the Fermi surfaces, and the interband Δ_{XY} and Δ_{YX} directly pair above/below the Fermi level. From Table III it can be seen that there exists no irreducible representation that is simultaneously intraband and interband, and thus no state that will open gaps both on the Fermi level and above/below the Fermi level. As an immediate consequence, all interband pairing states are disqualified. This is because interband pairing states will not open a gap at the Fermi level (save for at the Fermi surface crossings) for $T = T_c$; thus no superconducting instability exists in those channels.

In this scenario, intraband pairing is completely independent between the two electron pockets, with no term to mix the two pockets. The problem simplifies into two symmetry related one-band problems. A general property of one-band superconductors is the presence of the gap minimum above the original Fermi surfaces, i.e., back-bending, in agreement

TABLE III. Pairing symmetries with spin-orbit λ_z and without spin-orbit λ. Each pairing is listed with its irreducible symmetry representation and invariant coupling discussed in Sec. II B. (Notation: $\sigma_1 \equiv \sigma_X$, $\sigma_2 \equiv \sigma_Y$, and $\sigma_3 \equiv \sigma_z$.)

Intraband Δ_X, Δ_Y		
Pairing	Symmetry irrep.	Coupling
$1^T\tau_0 i\sigma_2 1$	A_{1g}	$U_1 + J'_{11}$
$3^T\tau_0 i\sigma_2 3$	A_{1g}	$U_3 + J'_{33}$
$1^T\tau_3 i\sigma_2 1$	B_{2g}	$U_1 - J'_{11}$
$3^T\tau_3 i\sigma_2 3$	B_{2g}	$U_3 - J'_{33}$
$1^T(\tau_0 \pm \tau_3) i\sigma_2 3$	E_u	$U'_{1X3X} + J_{1X3X}$
$1^T(\tau_0 \pm \tau_3)\sigma_2\sigma_3 3$	E_u	$U'_{1X3X} - J_{1X3X}$
$1^T(\tau_0 \pm \tau_3)\sigma_2\vec{\sigma} 3$	$E_u \times$ U(1)	$U'_{1X3X} - J_{1X3X}$
Interband Δ_{XY}, Δ_{YX}		
Pairing	Symmetry irrep.	Coupling
$1^T\tau_1 i\sigma_2 1$	A_{2u}	$U'_1 + J_{11}$
$3^T\tau_2 i\sigma_2\sigma_3 3$	A_{2u}	$U'_3 - J_{33}$
$3^T\tau_1 i\sigma_2 3$	B_{2u}	$U'_3 + J_{33}$
$1^T\tau_2 i\sigma_2\sigma_3 1$	B_{2u}	$U'_1 - J_{11}$
$1^T\tau_2 i\sigma_2\vec{\sigma} 1$	$B_{1u} \times$ U(1)	$U'_1 - J_{11}$
$3^T\tau_2 i\sigma_2\vec{\sigma} 3$	$A_{1u} \times$ U(1)	$U'_3 - J_{33}$
$1^T(\tau_1 \pm i\tau_2) i\sigma_2 3$	E_g	$U'_{1X3Y} + J_{1X3Y}$
$1^T(\tau_1 \pm i\tau_2)\sigma_2\sigma_3 3$	E_g	$U'_{1X3Y} - J_{1X3Y}$
$1^T(\tau_1 \pm i\tau_2)\sigma_2\vec{\sigma} 3$	$E_g \times$ U(1)	$U'_{1X3Y} - J_{1X3Y}$

TABLE IV. Pairing symmetries with spin-orbit λ: Ψ_1.

Pairing	Symmetry irrep.	Coupling
$1^T\tau_0 i\sigma_2 1$	A_{1g}	$U_1 + J'_{11}$
$3^T\tau_0 i\sigma_2 3$	A_{1g}	$U_3 + J'_{33}$
$1^T[(\tau_2 + i\tau_1)i + (\tau_2 - i\tau_1)\sigma_3]3$	A_{1g}	$U'_{1X3Y} - J_{1X3Y}$
$1^T\tau_3 i\sigma_2 1$	B_{2g}	$U_1 - J'_{11}$
$3^T\tau_3 i\sigma_2 3$	B_{2g}	$U_3 - J'_{33}$
$1^T[(\tau_2 + i\tau_1)(-i) + (\tau_2 - i\tau_1)\sigma_3]3$	B_{2g}	$U'_{1X3Y} - J_{1X3Y}$
$1^T[(\tau_2 + i\tau_1)\sigma_3 + (\tau_2 - i\tau_1)(-i)]3$	A_{2g}	$U'_{1X3Y} - J_{1X3Y}$
$1^T[(\tau_2 + i\tau_1)\sigma_3 + (\tau_2 - i\tau_1)i]3$	B_{1g}	$U'_{1X3Y} - J_{1X3Y}$
$1^T(\tau_0 \pm \tau_3)i\sigma_2 3$	E_u	$U'_{1X3X} + J_{1X3X}$
$1^T(\tau_0 \pm \tau_3)\sigma_2\sigma_3 3$	E_u	$U'_{1X3X} - J_{1X3X}$
$1^T\tau_2 i\sigma_2\vec{\sigma}1$	E_u	$U'_1 - J_{11}$
$3^T\tau_2 i\sigma_2\vec{\sigma}3$	E_u	$U'_3 - J_{33}$

TABLE V. Pairing symmetries with spin-orbit λ: Ψ_{2a} (Ψ_{2b}).

Pairing	Symmetry irrep.	Coupling
$1^T i[(\tau_0 + \tau_3)\sigma_3 + (\tau_0 - \tau_3)i]3$	A_{1u}	$U'_{1X3X} - J_{1X3X}$
$1^T i[(\tau_0 + \tau_3)i + (\tau_0 - \tau_3)\sigma_3]3$	B_{1u}	$U'_{1X3X} - J_{1X3X}$
$1^T i[(\tau_0 + \tau_3)(-i) + (\tau_0 - \tau_3)\sigma_3]3$	A_{2u}	$U'_{1X3X} - J_{1X3X}$
$1^T\tau_1 i\sigma_2 1$	A_{2u}	$U'_1 + J_{11}$
$3^T\tau_2 i\sigma_2\sigma_3 3$	A_{2u}	$U'_3 - J_{33}$
$1^T i[(\tau_0 + \tau_3)\sigma_3 + (\tau_0 - \tau_3)(-i)]3$	B_{2u}	$U'_{1X3X} - J_{1X3X}$
$3^T\tau_1 i\sigma_2 3$	B_{2u}	$U'_3 + J_{33}$
$1^T\tau_2 i\sigma_2\sigma_3 1$	B_{2u}	$U'_1 - J_{11}$
$1^T(\tau_1 \pm i\tau_2)i\sigma_2 3$	E_g	$U'_{1X3Y} + J_{1X3Y}$
$1^T(\tau_1 \pm i\tau_2)\sigma_2\sigma_3 3$	E_g	$U'_{1X3Y} - J_{1X3Y}$

with observations in the monolayer [7]. This leaves only the s- (A_{1g}), d- (B_{2g}), and p-wave [$E_u \times$ U(1)] pairing states in Table III.

However, STM experiments show a hard gap followed by not one but *two* peaks in the dI/dV, Fig. 3 [6]. The two peaks occur at 8.6 meV and 14.3 meV in intercalated ($Li_{1-x}Fe_x$)OHFeSe [6], and 9 meV and 20.1 meV in monolayer [18]. The suggestion that these two peaks come from the superconducting gap is at odds with monolayer ARPES, whose gap maximum is established to be less than 14 meV (even considering uncertainty) [7]. This suggests the presence of interband pairing, where the second peak originates from the gap opened above/below the Fermi level. In fact, without interband spin-orbit coupling, there is no way to produce a two-peak dI/dV spectrum. This is because the peaks are indicative of singularities in the density of states [24]. For an anisotropic superconductor these singularities come from the gap maximum, which is a saddle point. Two symmetry related one-band superconductors will each identically produce only one gap and thus only one gap maximum; thus only one peak would be measured by tunneling.

The simultaneous observation of interband phenomena [6,7,18] and the experimental constraints on the interband spin orbit ($\lambda \leqslant 5$ meV [7]) lend themselves towards the existence of a hierarchy. In this hierarchy, the leading order contribution to superconductivity comes from the intraband pairing states—s, d, and p wave—and where the introduction of a small interband spin-orbit coupling leads to an experimentally observed two-peak tunneling spectrum. The latter is primarily accomplished by the breaking of the SU(2) spin symmetry, which changes the symmetry of the spin-triplet pairs. This produces symmetry states of both intra- and interband character (see Tables IV and V), thus opening gaps above and below the Fermi level. Now a two-peak spectrum is possible, with the second peak coming from the gap opened above the Fermi level (such as is shown in Fig. 7).

We studied every possible pure symmetry state and found that only those states which contributed both intraband and interband pairing could generically meet our criteria: (i) nodeless, (ii) two-peak dI/dV spectrum, and (iii) back-bending. Further, because the pairing energy is of the order of half the difference in the band energies, we found that intraband pairing had to dominate in order to preserve the shape of the back-bending. Scenarios involving only interband pairing, or dominated by interband pairing, would result in a gap shifted off the normal state Fermi surface, and possibly even merged into a unified gap minimum in between the normal state Fermi surface. Of all symmetry derived pairings at the M point, only the s-, d-, and helical p-wave states could meet these criteria.

V. s WAVE

In this section we consider time-reversal invariant s-wave superconductivity, both with and without interband spin-orbit λ. Without spin-orbit λ the two electron pockets remain independent, and the problem reduces to two independent symmetry related one-band superconductors. Pairing within the electron pocket opens up a gap at the Fermi level; however, no interband pairing exists to open a gap above/below the Fermi level. We show that this scenario cannot produce the two-peak tunneling spectra, as there is no pairing above/below the Fermi level to open a second gap. To complicate matters further, the spin-singlet nature of the s-wave pairing has the

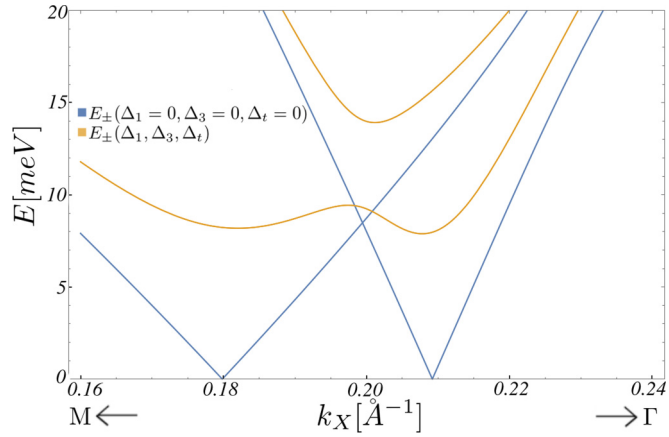

FIG. 7. Upper E_+ and lower E_- superconducting band in the ΓM direction for the A_{1g} state. The blue and yellow curves are the dispersions without and with pairing, respectively. In the presence of pairing, the lower band E_- has two local minima directly above the original Fermi surfaces. The lower and upper bands are split, with the largest contribution to the splitting coming from the interband pairing Δ_t. The parameters used are $\Delta_1 = 10.8$ meV, $\Delta_3 = 7.2$ meV, $\Delta_t = -3$ meV, $\lambda = 5$ meV, $\epsilon_1 = -45$ meV, $\epsilon_3 = -95$ meV, $\lambda_z = 26$ meV Å, and $p_{z1} = p_{z2} = 0$.

added theoretical problem of overcoming the large repulsive intraorbital Hubbard U (see Table III). Conveniently, the spin-orbit coupling λ provides a remedy to both these problems, by introducing an s-wave spin-triplet pair which pairs directly above/below the Fermi level. In this way, a fully gapped spectrum with a two-peak dI/dV and back-bending can be produced. Further, the introduced spin-triplet pair is attractive for (renormalized) Hund's J larger than the interorbital Hubbard U' and independent of the strength of intraorbital U.

The s-wave symmetry (A_{1g}) is invariant under all space group operations. Without the momentum-independent spin-orbit coupling λ, there are only two A_{1g} pairings: $1^T\Delta_1 i\sigma_2 1$ and $3^T\Delta_3 i\sigma_2 3$. Both pairings are of the intraband type, constituting two independent symmetry related one-band problems. Choosing to study the X pocket, we define the Nambu spinor $\Psi_X(\mathbf{k}) = (\psi_X^{\uparrow}(\mathbf{k}), \psi_X^{\downarrow\dagger}(-\mathbf{k}))^T$. The pairing Hamiltonian is then written as Eq. (14),

$$H_{BdG} = \sum_{\mathbf{k}} \Psi_X^{\dagger}(\mathbf{k}) \begin{pmatrix} h_X'^{\uparrow}(\mathbf{k}) & \hat{\Delta}_X \\ \hat{\Delta}_X & -h_X'^{\downarrow T}(-\mathbf{k}) \end{pmatrix} \Psi_X(\mathbf{k}), \quad (14)$$

where the $\hat{\Delta}_X$ is the constant 2×2 matrix

$$\hat{\Delta}_X = \begin{pmatrix} \Delta_1 & 0 \\ 0 & \Delta_3 \end{pmatrix}. \quad (15)$$

Noting that, because $h_X'^{\downarrow T}(-\mathbf{k}) = h_X'^{\uparrow}(\mathbf{k})$, Eq. (14) can be written as Eq. (16),

$$H_{BdG} = \sum_{\mathbf{k}} \Psi_X^{\dagger}(\mathbf{k}) \begin{pmatrix} h_X'^{\uparrow}(\mathbf{k}) & \hat{\Delta}_X \\ \hat{\Delta}_X & -h_X'^{\uparrow}(\mathbf{k}) \end{pmatrix} \Psi_X(\mathbf{k}). \quad (16)$$

The normal state Hamiltonian $h_X'^{\alpha}$ has two eigenvalues—one upward and one downward dispersing band. We project H_{BdG} onto the state which crosses the Fermi level, as discussed in Sec. II A:

$$H_{BdG} = \sum_{\mathbf{k}} \Psi_X^{\dagger}(\mathbf{k}) \begin{pmatrix} \epsilon_X(\mathbf{k}) & \Delta_X(\mathbf{k}) \\ \Delta_X(\mathbf{k}) & -\epsilon_X(\mathbf{k}) \end{pmatrix} \Psi_X(\mathbf{k}), \quad (17)$$

where the constant 2×2 matrix $\hat{\Delta}_X$ is reduced to a scalar function, inheriting its momentum dependence from the band structure,

$$\begin{aligned} \Delta_X(\mathbf{k}) &= \langle X\uparrow|\hat{\Delta}_X|X\uparrow\rangle \\ &= \frac{\Delta_1+\Delta_3}{2} + \frac{\Delta_1-\Delta_3}{2}\cos\theta. \end{aligned} \quad (18)$$

The pairing function Eq. (18) was previously studied by one of us in a previous work, Ref. [19]. In Eq. (17), $\Delta_X(\mathbf{k})$ directly mixes the particle and hole bands, thus opening a gap at the Fermi level. It can be seen from Eq. (18) that the gap anisotropy is centered about the average of the two order parameters Δ_1 and Δ_3, with fluctuations about the average proportional to the difference in the order parameters. If $\Delta_1 = \Delta_3$, the gap is isotropic. For fixed values of the order parameters such that $\Delta_1 \neq \Delta_3$, the fluctuations of the anisotropy about the average depends on $\cos\theta$. Since $\cos\theta$ measures the projection onto the polar axis of the Bloch sphere, which itself represents the reference states $M1$ and $M3$, the anisotropies fluctuate largest where the mixing between $M1$ and $M3$ is smallest (i.e., the $k_x = -k_y$ direction).

The pairing function for the second electron pocket $\Delta_Y(\mathbf{k})$ is a mirror image of $\Delta_X(\mathbf{k})$ under m_x, i.e., $\Delta_X(k_x,k_y) = \Delta_Y(-k_x,k_y)$. No mixing occurs between these two pockets, and no gap is opened above/below the Fermi level.

Pairing with spin-orbit coupling λ

The interband spin-triplet pairing $E_g \times \mathrm{U}(1)$ directly opens gaps above/below the Fermi level, but does not open any gap at the Fermi level. The momentum-independent spin-orbit coupling λ breaks the $E_g \times \mathrm{U}(1)$ spin-triplet state into four one-dimensional representations, one of which is A_{1g}. It is

$$\Delta_t 1_\alpha^T((\tau_2 + i\tau_1)i\delta^{\alpha\beta} + (\tau_2 - i\tau_1)\sigma_3^{\alpha\beta})3_\beta. \quad (19)$$

Spin singlets do not change symmetry with spin-orbit coupling; therefore, the two original pairings Δ_1 and Δ_3 remain A_{1g}. The problem becomes a full two-band superconductor, with the H_{BdG} written as

$$\begin{aligned} H_{BdG} = \sum_{\mathbf{k}} \Psi_1^{\dagger}(\mathbf{k}) &\begin{pmatrix} h_X'^{\uparrow}(\mathbf{k}) & \Lambda & \hat{\Delta}_X^{\dagger} & \hat{\Delta}_{YX}^{\dagger} \\ \Lambda^{\dagger} & h_X'^{\downarrow}(\mathbf{k}) & \hat{\Delta}_{XY}^{\dagger} & \hat{\Delta}_Y^{\dagger} \\ \hat{\Delta}_X & \hat{\Delta}_{XY} & -h_X'^{\uparrow}(\mathbf{k}) & -\Lambda \\ \hat{\Delta}_{YX} & \hat{\Delta}_Y & -\Lambda^{\dagger} & -h_X'^{\downarrow}(\mathbf{k}) \end{pmatrix} \\ &\times \Psi_1(\mathbf{k}), \end{aligned} \quad (20)$$

where the constant 2×2 pairing matrices are

$$\hat{\Delta}_X = \hat{\Delta}_Y = \begin{pmatrix} \Delta_1 & 0 \\ 0 & \Delta_3 \end{pmatrix} \quad (21)$$

and

$$\hat{\Delta}_{XY} = \hat{\Delta}_{YX}^{\dagger} = \Delta_t \begin{pmatrix} 0 & i \\ 1 & 0 \end{pmatrix}. \quad (22)$$

Defining the projector

$$\Gamma_1^{\dagger} = \begin{pmatrix} |X\uparrow\rangle & 0 & 0 & 0 \\ 0 & |Y\downarrow\rangle & 0 & 0 \\ 0 & 0 & |X\uparrow\rangle & 0 \\ 0 & 0 & 0 & |Y\downarrow\rangle \end{pmatrix} \quad (23)$$

allows us to project H_{BdG} onto the reduced band basis, as discussed in Sec. II A. This reduces the size of the Hilbert space by half, greatly simplifying the analysis. The Hilbert space is halved and the pairing Hamiltonian becomes

$$\begin{aligned} \mathcal{H}(\mathbf{k}) &\equiv \Gamma_1 H_{BdG}(\mathbf{k})\Gamma_1^{\dagger} \\ &= \begin{pmatrix} \epsilon_X(\mathbf{k}) & \lambda\kappa(\mathbf{k}) & \Delta_X(\mathbf{k}) & \Delta_t\kappa(\mathbf{k}) \\ \lambda\kappa^*(\mathbf{k}) & \epsilon_Y(\mathbf{k}) & \Delta_t\kappa^*(\mathbf{k}) & \Delta_Y(\mathbf{k}) \\ \Delta_X(\mathbf{k}) & \Delta_t\kappa(\mathbf{k}) & -\epsilon_X(\mathbf{k}) & -\lambda\kappa(\mathbf{k}) \\ \Delta_t\kappa^*(\mathbf{k}) & \Delta_Y(\mathbf{k}) & -\lambda\kappa^*(\mathbf{k}) & -\epsilon_Y(\mathbf{k}) \end{pmatrix}. \end{aligned} \quad (24)$$

The function $\kappa(\mathbf{k})$ is defined as the projection

$$\kappa(\mathbf{k}) = \langle X\uparrow| \begin{pmatrix} 0 & i \\ 1 & 0 \end{pmatrix} |Y\downarrow\rangle. \quad (25)$$

The phase on the interband mixing $\lambda\kappa$ and the interband pairing $\Delta_t\kappa$ both come from $\kappa(k)$. There is no relative phase between the two; thus it is possible to define a unitary transform

Eq. (26) which completely eliminates the phase,

$$V_1 = \begin{pmatrix} \frac{\kappa^*}{|\kappa|} & 0 & 0 & 0 \\ 0 & 1 & 0 & 0 \\ 0 & 0 & \frac{\kappa^*}{|\kappa|} & 0 \\ 0 & 0 & 0 & 1 \end{pmatrix}. \tag{26}$$

Rotating $\mathcal{H}$ into the new basis via $V_1 \mathcal{H} V_1^\dagger$ produces

$$\mathcal{H}(\mathbf{k}) = \begin{pmatrix} \epsilon_X & \lambda|\kappa| & \Delta_X & \Delta_t|\kappa| \\ \lambda|\kappa| & \epsilon_Y & \Delta_t|\kappa| & \Delta_Y \\ \Delta_X & \Delta_t|\kappa| & -\epsilon_X & -\lambda|\kappa| \\ \Delta_t|\kappa| & \Delta_Y & -\lambda|\kappa| & -\epsilon_Y \end{pmatrix}. \tag{27}$$

Let τ_i and σ_i be Pauli matrices; the 4×4 Hamiltonian Eq. (27) can be written in the convenient form

$$\mathcal{H} = \tau_3(A + B_3\sigma_3 + B_1\sigma_1) + \tau_1(C + D_3\sigma_3 + D_1\sigma_1), \tag{28}$$

where $A = \frac{1}{2}(\epsilon_X + \epsilon_Y)$, $B_3 = \frac{1}{2}(\epsilon_X - \epsilon_Y)$, $B_1 = \lambda|\kappa|$, $C = \frac{1}{2}(\Delta_X + \Delta_Y)$, $D_3 = \frac{1}{2}(\Delta_X - \Delta_Y)$, and $D_1 = \Delta_t|\kappa|$. And for convenience $B = \sqrt{B_1^2 + B_3^2}$ and $D = \sqrt{D_1^2 + D_3^2}$. The eigenvalues of Eq. (28) are the superconducting dispersion:

$$E_\pm^2 = A^2 + B^2 + C^2 + D^2 \pm 2\sqrt{(AB_3 + CD_3)^2 + (AB_1 + CD_1)^2 + (B_1D_3 - B_3D_1)^2}. \tag{29}$$

Because of the two-band nature of this superconductor, there are two distinct superconducting bands—one upper and one lower. The "upper" and "lower" band are defined by $E_+(\mathbf{k}) > E_-(\mathbf{k})$ for any momentum $\mathbf{k} \in \mathbb{R}_2$. The superconducting gap is the difference between the lower band E_- and the Fermi level, which occurs due to intraband pairing. In general, a second gap exists between the two superconducting bands, defined by $E_+(\mathbf{k}) - E_-(\mathbf{k})$. The splitting $E_+(\mathbf{k}) - E_-(\mathbf{k})$ depends entirely on interband pairing, which can come indirectly from Δ_X and Δ_Y through λ, or directly from Δ_t. In Fig. 8 we plot the density of states, which is probed by tunneling experiments. Two peaks occur in the spectrum, each from saddle points on the upper and lower superconducting bands. We further plot the dispersion in the ΓM direction for the same parameters, Fig. 7, showing the gap lies above the original Fermi surfaces.

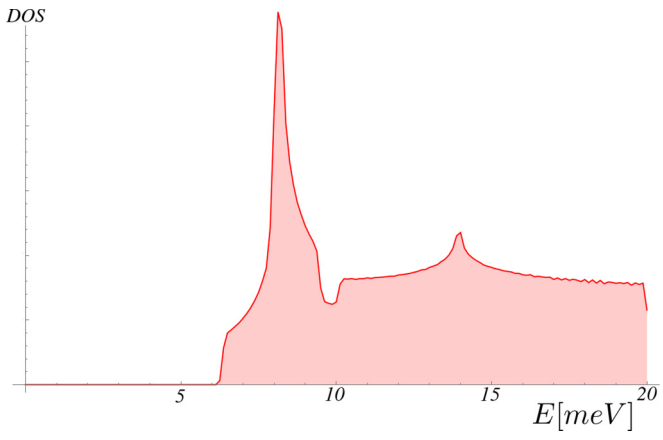

FIG. 8. Density of states for the A_{1g} state, numerically calculated using the full 8×8 Hamiltonian Eq. (20). Two peaks are present—the first coming from the intraband pairing gap and the second coming from interband pairing above the Fermi level. The few states below the first peak come from the gap minimum, which lies in the direction of the crossing. The same parameters are used as in Fig. 7. [*Please note*: a phenomenological scattering model (e.g., Dynes model) was *not* implemented here. Such a model would smooth out the peaks but introduce states into the gap.]

VI. *d* WAVE

The d-wave symmetry is defined by a sign change under a 90° rotation. There are two crystallographic symmetry representations that have this property: B_{2g} and B_{1g}. The B_{1g} representation has one interband pairing state, which only appears in the presence of spin-orbit λ. There are no B_{1g} intraband pairing states, and thus B_{1g} cannot reproduce the back-bending reported in experiments. On the other hand, the B_{2g} representation has two intraband pairing states when $\lambda = 0$: $1^T\Delta_1\tau_3 i\sigma_2 1$ and $3^T\Delta_3\tau_3 i\sigma_2 3$. Further, in the presence of λ, the B_{2g} state picks up a spin-orbit coupled triplet state. This state is an interband pairing state, which directly opens a gap above/below the Fermi level. Thus the B_{2g} symmetry representation can produce a two-peak dI/dV spectrum while preserving back-bending.

In this section we consider time-reversal invariant B_{2g} superconductivity in the presence of interband spin-orbit λ. As with s-wave superconductivity, without spin-orbit λ the two electron pockets remain independent, and the problem reduces to two independent symmetry related one-band superconductors. Similarly, the spin-singlet d-wave states have the added problem of overcoming the large intraorbital Hubbard U. In fact, without spin-orbit λ the d-wave and s-wave problems are identical, save the d-wave superconductor changes sign between pockets. As such, we will not repeat this discussion; we instead point the reader to Sec. V.

Two important changes occur with the introduction of spin-orbit λ. First is the introduction of an interband spin-triplet pairing state, Eq. (30). Similar to the A_{1g} triplet state discussed in Sec. V, the B_{2g} triplet pair comes from the reduction of the $E_g \times \mathrm{U}(1)$ state into one-dimensional representations:

$$\Delta_t 1_\alpha^T((\tau_2 + i\tau_1)(-i)\delta^{\alpha\beta} + (\tau_2 - i\tau_1)\sigma_3^{\alpha\beta})3_\beta. \tag{30}$$

The second important change is to the band structure. The spin-orbit coupling λ is of the interband type, mixing $h_X'^\alpha$ and $h_Y'^\beta$ bands (for $\alpha \neq \beta$), and avoiding the electron pocket crossing (see Fig. 5). Because the B_{2g} state changed sign between the original electron pockets, the mixing of the pockets at the crossing demands symmetry required nodes there. More precisely, two nodes exist at every crossing, one each on the inner and outer pocket. However, because of the large size

of the superconducting gap [6,7,16] and the experimentally constrained size of λ [7], the two nodes merge and open up a gap. Theoretically, the merging of Dirac gap nodes has already been studied in the context of hole pockets[25,26] and in electron pockets of monolayer FeSe [22].

The pairing matrix H_{BdG} is written

$$H_{BdG} = \sum_{\mathbf{k}} \Psi_1^\dagger(\mathbf{k}) \begin{pmatrix} h_X'^{\uparrow}(\mathbf{k}) & \Lambda & \hat{\Delta}_X^\dagger & \hat{\Delta}_{YX}^\dagger \\ \Lambda^\dagger & h_X'^{\downarrow}(\mathbf{k}) & \hat{\Delta}_{XY}^\dagger & \hat{\Delta}_Y^\dagger \\ \hat{\Delta}_X & \hat{\Delta}_{XY} & -h_X'^{\uparrow}(\mathbf{k}) & -\Lambda \\ \hat{\Delta}_{YX} & \hat{\Delta}_Y & -\Lambda^\dagger & -h_X'^{\downarrow}(\mathbf{k}) \end{pmatrix} \times \Psi_1(\mathbf{k}), \tag{31}$$

where the constant 2×2 pairing matrices are

$$\hat{\Delta}_X = -\hat{\Delta}_Y = \begin{pmatrix} \Delta_1 & 0 \\ 0 & \Delta_3 \end{pmatrix} \tag{32}$$

and

$$\hat{\Delta}_{XY} = \hat{\Delta}_{YX}^\dagger = \Delta_t \begin{pmatrix} 0 & i \\ -1 & 0 \end{pmatrix}. \tag{33}$$

Projecting onto the reduced band basis via the projector Eq. (23) produces

$$\mathcal{H}(\mathbf{k}) \equiv \Gamma_1 H_{BdG}(\mathbf{k}) \Gamma_1^\dagger = \begin{pmatrix} \epsilon_X(\mathbf{k}) & \lambda\kappa(\mathbf{k}) & \Delta_X(\mathbf{k}) & \Delta_t\gamma(\mathbf{k}) \\ \lambda\kappa^*(\mathbf{k}) & \epsilon_Y(\mathbf{k}) & \Delta_t\gamma^*(\mathbf{k}) & \Delta_Y(\mathbf{k}) \\ \Delta_X(\mathbf{k}) & \Delta_t\gamma(\mathbf{k}) & -\epsilon_X(\mathbf{k}) & -\lambda\kappa(\mathbf{k}) \\ \Delta_t\gamma^*(\mathbf{k}) & \Delta_Y(\mathbf{k}) & -\lambda\kappa^*(\mathbf{k}) & -\epsilon_Y(\mathbf{k}) \end{pmatrix}. \tag{34}$$

Again, $\kappa(\mathbf{k})$ is defined as the projection Eq. (25). Further, we defined a second projection,

$$\gamma(\mathbf{k}) = \langle X\uparrow | \begin{pmatrix} 0 & i \\ -1 & 0 \end{pmatrix} | Y\downarrow \rangle, \tag{35}$$

noting that in the Bloch sphere coordinates $\gamma(\theta,\phi) = \kappa^*(\theta,\pi-\phi)$.

Important to the symmetry of the superconductor is the relative phase between the interband spin-orbit coupling $\lambda\kappa$ and the interband pairing $\Delta_t\gamma$. It is in the difference in the phase between κ and γ that the symmetry arises. Applying unitary transform Eq. (26) pushes the phase from the spin-orbit coupling onto the pairing, simplifying this picture:

$$\mathcal{H}(\mathbf{k}) = \begin{pmatrix} \epsilon_X & \lambda|\kappa| & \Delta_X & \Delta_t\frac{\kappa^*}{|\kappa|}\gamma \\ \lambda|\kappa| & \epsilon_Y & \Delta_t\frac{\kappa}{|\kappa|}\gamma^* & \Delta_Y \\ \Delta_X & \Delta_t\frac{\kappa^*}{|\kappa|}\gamma & -\epsilon_X & -\lambda|\kappa| \\ \Delta_t\frac{\kappa}{|\kappa|}\gamma^* & \Delta_Y & -\lambda|\kappa| & -\epsilon_Y \end{pmatrix}. \tag{36}$$

If we let τ_i and σ_i be Pauli matrices, the 4×4 Hamiltonian Eq. (36) can be written in the convenient form

$$\mathcal{H} = \tau_3(A + B_3\sigma_3 + B_1\sigma_1) + \tau_1(C + D_3\sigma_3 + D_1\sigma_1 + D_2\sigma_2), \tag{37}$$

where $A = \frac{1}{2}(\epsilon_X + \epsilon_Y)$, $B_3 = \frac{1}{2}(\epsilon_X - \epsilon_Y)$, $B_1 = \lambda|\kappa|$, $C = \frac{1}{2}(\Delta_X + \Delta_Y)$, $D_3 = \frac{1}{2}(\Delta_X - \Delta_Y)$, $D_1 = \Delta_t \mathrm{Re}(\frac{\kappa}{|\kappa|}\gamma^*)$, and $D_2 = \Delta_t \mathrm{Im}(\frac{\kappa}{|\kappa|}\gamma^*)$, and for convenience $B = \sqrt{B_1^2 + B_3^2}$ and $D = \sqrt{D_1^2 + D_2^2 + D_3^2}$. The superconducting dispersion is thus:

$$E_\pm^2 = A^2 + B^2 + C^2 + D^2 \pm 2((AB_3 + CD_3 - B_1D_2)^2 + (AB_1 + CD_1 + B_3D_2)^2 + (B_1D_3 - B_3D_1 + CD_2)^2)^{1/2}. \tag{38}$$

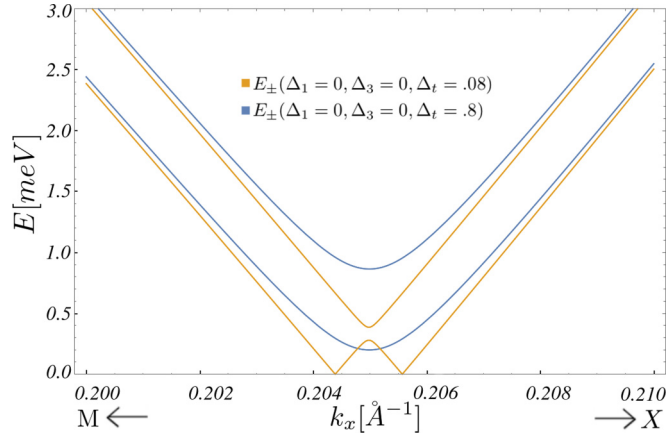

FIG. 9. Superconducting dispersion in the MX direction for $\Delta_t = 0.08$ meV (yellow) and $\Delta_t = 0.8$ meV (blue), and with interband spin-orbit $\lambda = 0.5$ meV. For $\Delta < \lambda$, two Dirac gap nodes lie along the $k_x > 0$ line. Interband pairing opens a gap above the Fermi level. Increasing Δ_t grows the gap above the Fermi level, pulling the Dirac nodes together. For $\Delta_t > 0.5$ meV, the nodes merge and open a gap.

The d-wave symmetry changes sign under 90° rotations. For the B_{2g} representation, this implies the inner and outer pockets change sign in the direction of the avoided Fermi surface crossings. Thus this requires the existence of Dirac gap nodes. However, this is only true so long as the pairing energy is less than half the difference in the band energies. In the direction of the crossing, half the difference in the band energies is equal to λ. In Fig. 9 we plot the superconducting gap in the direction of the crossing. For values of Δ_1, Δ_3, and Δ_t less than spin-orbit λ, there exists two Dirac gap nodes. As the pairing parameters increase, the gap above/below the Fermi level grows. This pushes the nodes closer together, annihilating them for Δ's larger than spin-orbit λ.

In Fig. 10 we plot the density of states showing a two-peak spectrum. The first peak comes from the saddle point in the superconducting gap, while the second peak comes from a saddle point in the upper superconducting band $E_+(\mathbf{k})$. The dispersion in the ΓM direction is plotted in Fig. 11 for the same parameters used to produce the two peaks, showing the presence of back-bending above the original Fermi surfaces.

VII. HELICAL p WAVE

The p-wave symmetry is characterized by its sign change under inversion. Without interband spin-orbit coupling λ, there exists two p-wave symmetries: E_u and $E_u \times \mathrm{U}(1)$. The irreducible symmetry representation E_u is also the in-plane polar vector representation (k_x,k_y). The representation labeled purely E_u—composed of one spin singlet and one spin triplet with $\vec{d}$ vector pointing out of plane—is nodal. Thus we shift out attention to the second symmetry representation $E_u \times \mathrm{U}(1)$. This representation is an orbital E_u spin triplet, with the

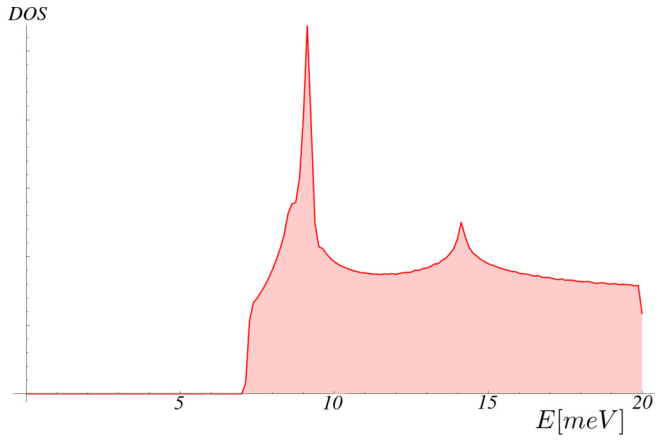

FIG. 10. Density of states for the B_{2g} state, numerically calculated using the full 8×8 Hamiltonian Eq. (31). Two peaks are present—the first coming from the intraband pairing gap and the second coming from interband pairing above the Fermi level. The same parameters are used as in Fig. 11. [*Please note*: a phenomenological scattering model (e.g., Dynes model) was *not* implemented here. Such a model would smooth out the peaks but introduce states into the gap.]

$\vec{d}$ vector pointing in plane. The continuous U(1) symmetry represents the freedom to rotate the triplet's $\vec{d}$ vector about the z axis. This representation

$$1_\alpha^T \Delta_\pm(\tau_0 \pm \tau_3)(\sigma_2\vec{\sigma})^{\alpha\beta}3_\beta \tag{39}$$

is a *fully gapped* time-reversal invariant topological superconductor. Its sign change under inversion owes itself to the action of spinors under the generators of symmetry.

Because Eq. (39) is an intraband pairing, pairing directly on the Fermi level, with no mixing between the independent electron pockets, this problem decouples into two one-band problems. Further, since Eq. (39) pairs electrons with the same spin on the same band, we are forced to define a Nambu spinor with doubled degrees of freedom $\Psi_{X\uparrow}(\mathbf{k}) = (\psi_X^{\uparrow}(\mathbf{k}), \psi_X^{\uparrow\dagger}(-\mathbf{k}))^T$. This doubling of the degrees of freedom can be corrected by constraining momentum $\mathbf{k}$ to half the Brillouin zone. In this way the spinors $\psi_X^{\uparrow}(\mathbf{k})$ and $\psi_X^{\uparrow\dagger}(-\mathbf{k})$ are completely decoupled, and the anticommutation relation Eq. (40) is satisfied:

$$\{\psi_X^{\uparrow}(\mathbf{k}), \psi_X^{\uparrow\dagger}(-\mathbf{k})\} = 0. \tag{40}$$

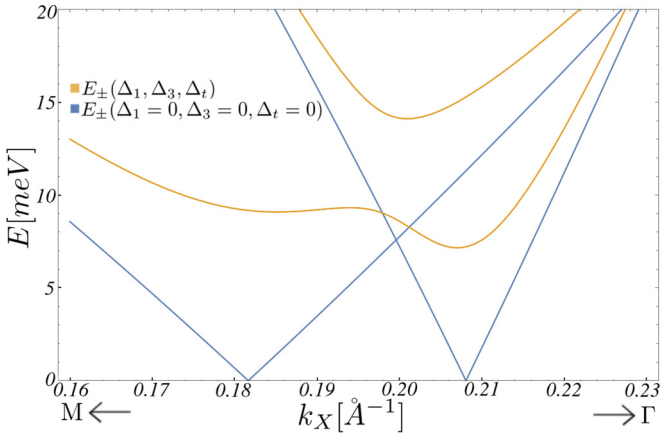

FIG. 11. Upper E_+ and lower E_- superconducting band in the ΓM direction for the B_{2g} state. The blue and yellow curves are the dispersions without and with pairing, respectively. In the presence of pairing, the lower band E_- has two local minima directly above the original Fermi surfaces. The lower and upper bands are split, with the largest contribution to the splitting coming from the interband pairing Δ_t. The parameters used are $\Delta_1 = 10.8$ meV, $\Delta_3 = 7.2$ meV, $\Delta_t = -4.8$ meV, $\lambda = 0.5$ meV, $\epsilon_1 = -45$ meV, $\epsilon_3 = -95$ meV, $\lambda_z = 26$ meV Å, and $p_{z1} = p_{z2} = 0$.

Because of the presence of time-reversal symmetry, it is not enough to consider only the spin-up particles. A second spinor $\Psi_{X\downarrow}(\mathbf{k}) = (\psi_X^{\downarrow}(\mathbf{k}), \psi_X^{\downarrow\dagger}(-\mathbf{k}))^T$ exists. Using these spinors, the pairing Hamiltonian is

$$\begin{aligned} H_{BdG} = &\sum_{\mathbf{k}} \Psi_{X\uparrow}^\dagger(\mathbf{k}) \begin{pmatrix} h_X'^{\uparrow}(\mathbf{k}) & \hat{\Delta}_{X\uparrow}^\dagger \\ \hat{\Delta}_{X\uparrow} & -h_X'^{\uparrow}(-\mathbf{k})^T \end{pmatrix} \Psi_{X\uparrow}(\mathbf{k}) \\ &+ \Psi_{X\downarrow}^\dagger(\mathbf{k}) \begin{pmatrix} h_X'^{\downarrow}(\mathbf{k}) & \hat{\Delta}_{X\downarrow}^\dagger \\ \hat{\Delta}_{X\downarrow} & -h_X'^{\downarrow}(-\mathbf{k})^T \end{pmatrix} \Psi_{X\downarrow}(\mathbf{k}). \end{aligned} \tag{41}$$

Using the fact that $h_X'^{\uparrow}(-\mathbf{k})^T = h_X'^{\downarrow}(\mathbf{k})$, we write

$$\begin{aligned} H_{BdG} &= H_{BdG\uparrow} + H_{BdG\downarrow} \\ &= \sum_k \Psi_{X\uparrow}^\dagger(\mathbf{k}) \begin{pmatrix} h_X'^{\uparrow}(\mathbf{k}) & \hat{\Delta}_{X\uparrow}^\dagger \\ \hat{\Delta}_{X\uparrow} & -h_X'^{\downarrow}(\mathbf{k}) \end{pmatrix} \Psi_{X\uparrow}(\mathbf{k}) \\ &\quad + \Psi_{X\downarrow}^\dagger(\mathbf{k}) \begin{pmatrix} h_X'^{\downarrow}(\mathbf{k}) & \hat{\Delta}_{X\downarrow}^\dagger \\ \hat{\Delta}_{X\downarrow} & -h_X'^{\uparrow}(\mathbf{k}) \end{pmatrix} \Psi_{X\downarrow}(\mathbf{k}). \end{aligned} \tag{42}$$

The U(1) spin symmetry gives us the freedom to choose any in-plane direction for the $\vec{d}$ vector. We choose to point the $\vec{d}$ vector in the y direction, writing

$$\hat{\Delta}_{X\uparrow} = \hat{\Delta}_{X\downarrow} = \begin{pmatrix} 0 & \Delta_+ \\ -\Delta_+ & 0 \end{pmatrix}. \tag{43}$$

Under time reversal spin-up and spin-down particles map into one another as $\psi_{X\uparrow}(\mathbf{k}) \to \psi_\downarrow(-\mathbf{k})$ and $\psi_{X\downarrow}(\mathbf{k}) \to -\psi_\uparrow(-\mathbf{k})$; this is followed by a complex conjugation. For this choice of $\vec{d}$ vector $\hat{\Delta}_{X\uparrow} = \hat{\Delta}_{X\downarrow}$ are real matrices. As a consequence, under time reversal $\psi_{X\uparrow}^T(-\mathbf{k})\hat{\Delta}_{X\uparrow}\psi_{X\uparrow}(\mathbf{k})$ and $\psi_{X\downarrow}^T(-\mathbf{k})\hat{\Delta}_{X\downarrow}\psi_{X\downarrow}(\mathbf{k})$ map into one another exactly. Thus the $E_u \times$ U(1) pairing is time-reversally symmetric.

Not only is this pairing time-reversally symmetric, it is fully gapped. In order to show this, it is enough to consider only $H_{BdG\uparrow}$. This is because $H_{BdG\uparrow}$ and $H_{BdG\downarrow}$ are related by time reversal and share no cross terms. Defining $\mathcal{H}_\uparrow$ to be the projection of $H_{BdG\uparrow}$ onto the bands that cross the Fermi level, we produce Eq. (44):

$$\mathcal{H}_\uparrow(\mathbf{k}) = \begin{pmatrix} \epsilon_X(\mathbf{k}) & \Delta_{X\uparrow}^*(\mathbf{k}) \\ \Delta_{X\uparrow}(\mathbf{k}) & -\epsilon_X(\mathbf{k}) \end{pmatrix}. \tag{44}$$

Projecting the 2×2 constant pairing matrices Eq. (43) into this basis reduces them to scalar functions $\Delta_{X\uparrow}(k)$ and $\Delta_{X\downarrow}(k)$. The momentum dependence of these scalar functions is inherited from the $\epsilon_X(k)$ band structure. Inheriting their symmetry from the band structure, the up-spin and down-spin pairing functions are related by $\Delta_{X\uparrow}(\theta,\phi) = \Delta_{X\downarrow}(\theta,\pi - \phi)$,

where $\Delta_{X\uparrow}(\mathbf{k})$ in Bloch coordinates $(\theta(\mathbf{k}),\phi(\mathbf{k}))$ is

$$\Delta_{X\uparrow}(\mathbf{k}) \equiv \langle X\downarrow|\hat{\Delta}_{X\uparrow}|X\uparrow\rangle = -\sin\theta\, e^{-i\phi}\Delta_+. \tag{45}$$

The form factor of Eq. (45) is the azimuthal projection of $\hat{\mathbb{h}}$ onto the Bloch sphere. Recall that in the Bloch representation $\hat{\mathbb{h}} = \tau_3\cos\theta + \sin\theta(\tau_1\cos\phi + \tau_2\sin\phi)$. As a consequence of the spin-orbit λ_z, the projection onto the azimuthal plane of the Bloch sphere is always nonzero. Thus the pairing function $\Delta_{X\uparrow}(\mathbf{k})$ [and by extension $\Delta_{X\downarrow}(\mathbf{k})$] is nodeless.

This state $E_u \times \mathrm{U}(1)$ is rather novel. While for $\lambda = 0$ the s-wave, d-wave, and p-wave states can produce a full gap at the Fermi level, the p-wave state is the only state which does not have to fight the large intraorbital repulsion. The spin-triplet nature of the pair provides a pathway for stabilization via the Hund's term. The Bloch-Kanamori couplings are listed with their symmetry (for $\lambda = 0$) in Table III. The coupling for the $E_u \times \mathrm{U}(1)$ state is $U'_{1X3X} - J_{1X3X}$, which is attractive when the Hund's term J_{1X3X} is greater than the interorbital Coulomb repulsion U'_{1X3X}.

With spin-orbit λ

As discussed in Sec. IV, with $\lambda = 0$ the p-wave state is a one-band problem. This generically leads to gaps opening on the Fermi level but never above/below the Fermi level. Consequently, the dI/dV spectrum will only have one peak at the energy of the gap maximum. Turning on the momentum-independent spin-orbit λ resolves this problem. With finite λ, the full spin symmetry is broken. This breaks the $E_u \times \mathrm{U}(1)$ state into four one-dimensional representations, which are listed in Table V: A_{1u}, B_{1u}, A_{2u}, and B_{2u}. Two of these representations—A_{2u} and B_{2u}—contribute two interband pairing states which pair directly above/below the Fermi level. The combination of intraband triplet and interband singlets has the ability to produce a two-peak dI/dV spectrum and back-bending.

The A_{2u} and B_{2u} representations are similar; thus it will suffice to discuss the A_{2u} pairing. The three A_{2u} pairings are listed in Table V. The two interband pairings are $1^T\Delta_1\tau_1 i\sigma_2 1$ and $3^T\Delta_3\tau_2 i\sigma_2\sigma_3 3$. The spin-triplet coming from the reduction of $E_u \times \mathrm{U}(1)$ is

$$\Delta_t 1^T_\alpha((\tau_0+\tau_3)\delta^{\alpha\beta} + (\tau_0-\tau_3)i\sigma_3^{\alpha\beta})3_\beta. \tag{46}$$

The A_{2u} representation is odd under in-plane mirror m_z; thus the pairing Hamiltonian Eq. (47) is written using the $\Psi_{2a}(\mathbf{k})$ and $\Psi_{2b}(\mathbf{k})$ Nambu spinors. As with the $\lambda = 0$ scenario, we avoid the doubling of degrees of freedom by constraining momentum to half the Brillouin zone. This decouples the $\psi_{X\uparrow}(\mathbf{k})$ and $\psi_{X\uparrow}(-\mathbf{k})$ components, satisfying the anticommutation relation Eq. (40):

$$H_{BdG} = H_{BdGa} + H_{BdGb} = \sum_{\mathbf{k}} \Psi^\dagger_{2a}(\mathbf{k}) \begin{pmatrix} h'^{\uparrow}_X(\mathbf{k}) & \Lambda & \hat{\Delta}^\dagger_X & \hat{\Delta}^\dagger_{YX} \\ \Lambda^\dagger & h'^{\downarrow}_Y(\mathbf{k}) & \hat{\Delta}^\dagger_{XY} & \hat{\Delta}^\dagger_Y \\ \hat{\Delta}_X & \hat{\Delta}_{XY} & -h'^{\downarrow}_X(\mathbf{k}) & \Lambda^* \\ \hat{\Delta}_{YX} & \hat{\Delta}_Y & \Lambda^T & -h'^{\uparrow}_Y(\mathbf{k}) \end{pmatrix} \Psi_{2a}(\mathbf{k}) + \Psi^\dagger_{2b}(\mathbf{k}) \begin{pmatrix} h'^{\downarrow}_X(\mathbf{k}) & -\Lambda^* & \hat{\Delta}^\dagger_X & -\hat{\Delta}^T_{YX} \\ -\Lambda^T & h'^{\uparrow}_Y(\mathbf{k}) & -\hat{\Delta}^T_{XY} & -\hat{\Delta}^\dagger_Y \\ \hat{\Delta}_X & -\hat{\Delta}^*_{XY} & -h'^{\uparrow}_X(\mathbf{k}) & -\Lambda \\ -\hat{\Delta}^*_{YX} & -\hat{\Delta}_Y & -\Lambda^\dagger & -h'^{\downarrow}_Y(\mathbf{k}) \end{pmatrix} \times \Psi_{2b}(\mathbf{k}). \tag{47}$$

The 2×2 constant intraband pairing matrices are

$$\hat{\Delta}_X = \Delta_t \begin{pmatrix} 0 & 1 \\ -1 & 0 \end{pmatrix} \tag{48}$$

and

$$\hat{\Delta}_Y = \Delta_t \begin{pmatrix} 0 & i \\ -i & 0 \end{pmatrix}. \tag{49}$$

The 2×2 constant interband pairing matrices are

$$\hat{\Delta}_{XY} = \hat{\Delta}_{YX} = \begin{pmatrix} \Delta_1 & 0 \\ 0 & i\Delta_3 \end{pmatrix}. \tag{50}$$

The pairing Hamiltonian H_{BdGa} maps to H_{BdGb} under time reversal. The two Hamiltonians share no cross terms and are otherwise independent. Thus it is sufficient to focus on H_{BdGa} in studying the superconducting gap structure. Numerical diagonalization of the full 8×8 $H_{BdGa}(\mathbf{k})$ shows two superconducting bands near the Fermi surface, which we refer to as the "upper" $E_+(\mathbf{k})$ and "lower" $E_-(\mathbf{k})$ bands. Plots of both the dispersion in the ΓM direction, Fig. 12, and the density of states, Fig. 13, show both back-bending and a two-peak tunneling spectrum. The two peaks in the spectrum come from saddle points on both the upper and lower superconducting bands. As with the s- and d-wave scenarios, the requirement that there be back-bending implies the dominance of the intraband pairing. Unlike the s- and d-wave scenarios, however, the dominant intraband pairing for the p-wave state is a spin triplet. As mentioned previously, spin-triplet pairs are attractive when the (renormalized) Hund's J overcomes the interorbital Hubbard U', independent of the strength of the intraorbital U. For the dominant (i.e., the intraband) pairing to be spin-triplet supports a hypothesis in which the pairing in this channel is stabilized by the Hund's term.

VIII. CONCLUSION

The constraint on the size of the interband mixing ($\lambda \leqslant 5$ meV) from ARPES on the monolayer [7] and bulk [13] suggests the superconducting state and gap in the FeSe's is dominated, to leading order, by pairing *within* two independent electron pockets at M (i.e., intraband pairing). However, the presence of a two-peak dI/dV STM spectrum [6,18] in the su-

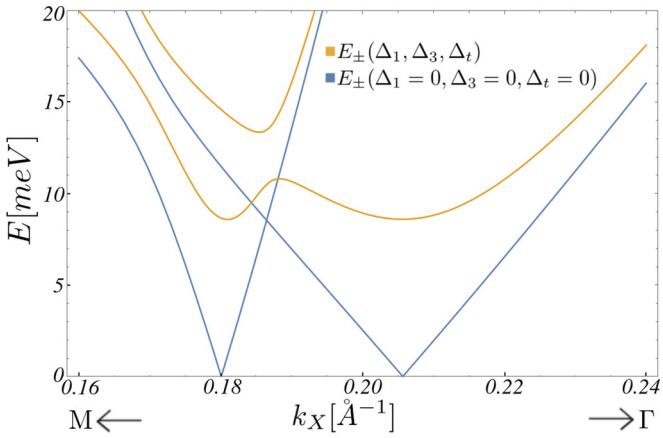

FIG. 12. Upper E_+ and lower E_- superconducting band in the ΓM direction for the A_{2u} state. The blue and yellow curves are the dispersions without and with pairing, respectively. In the presence of pairing, the lower band E_- has two local minima directly above the original Fermi surfaces. The lower and upper bands are split, with the largest contribution to the splitting coming from the interband pairing Δ_1 and Δ_3. The parameters used are $\Delta_1 = 6$ meV, $\Delta_3 = 7$ meV, $\Delta_t = -9$ meV, $\lambda = 3$ meV, $\epsilon_1 = -55$ meV, $\epsilon_3 = -105$ meV, $\lambda_z = -31.968$ meV Å, $p_{z1} = 4178.88$ meV Å^3, and $p_{z2} = 2.5 p_{z1}$.

perconducting state strongly implies the presence of interband pairing, which is necessary to open a sizable gap at the band crossing above/below the Fermi level. We studied all symmetry derived order parameters at the M point in the absence of interband mixing through the interband spin-orbit coupling λ, and found that no single pairing symmetry simultaneously opens gaps at the Fermi level and above/below the Fermi level (see Table III). Three states open a full gap centered above the original Fermi surfaces—s-, d-, and helical p-wave intraband

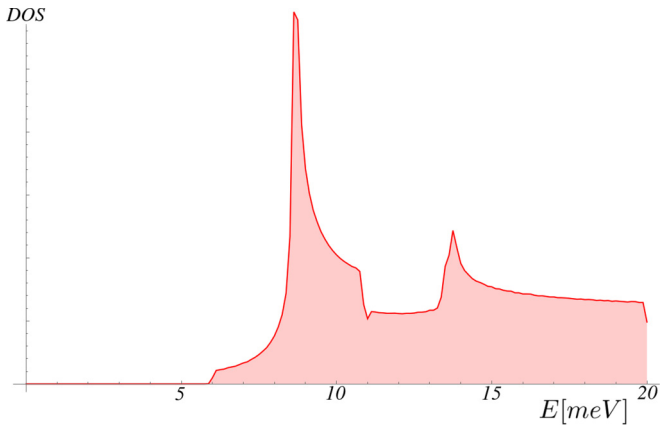

FIG. 13. Density of states for the A_{2u} state, numerically calculated using the full 8×8 Hamiltonian H_{BdGa} in Eq. (47). Two peaks are present—the first coming from the intraband pairing gap and the second coming from interband pairing above the Fermi level. The few states below the first peak come from the gap minimum, which lies in the direction of the crossing. The same parameters are used as in Fig. 12. [*Please note*: a phenomenological scattering model (e.g., Dynes model) was *not* implemented here. Such a model would smooth out the peaks but introduce states into the gap.]

pairing states—but open no gap above/below the Fermi level, and thus cannot reproduce the second tunneling peak [6,18]. The introduction of a *small* interband spin-orbit coupling resolves this problem by breaking the SU(2) spin symmetry, which changes the symmetry of spin-triplet pairs, and leads to symmetry states of mixed inter- and intraband pairing character. We further studied all possible pairing symmetries in this scenario (see Tables IV and V), and found that only those symmetry states with intra- and interband pairing, where the intraband pairing dominated, was able to meet out criteria: (i) full superconducting gap [6,7,16,18], (ii) gap centered above original Fermi surface (i.e., back-bending), and (iii) two-peak local density of states (corresponding to a two-peak dI/dV tunneling spectrum [6,18]). These states are the s-, d-, and helical p-wave intraband pairing states, where interband spin-orbit coupling λ mixes in some interband pairing, leading to a two-peak spectrum as a subleading effect.

The connection between the symmetry of the order parameter and the (renormalized) Hubbard-Hund's interactions highlights the detrimental role of the intra- and interorbital Hubbard repulsion, U and U', and the beneficial role of the pair-hopping and Hund's interactions, J' and J. In particular it reveals that, in the scenario without a small interband mixing, the spin-singlet s- and d-wave pairing states fight the large intraorbital Hubbard U, while the spin-triplet helical p-wave state benefits from the possibility of an attractive interaction when $U' < J$, completely avoiding the large repulsive intraorbital U (as was shown for hole pockets in Ref. [20]). However, with the introduction of a small interband spin-orbit λ, all three qualifying symmetry states (s, d, and helical p wave) receive contributions from spin-triplet pairs, and thus all three have an attractive mechanism when $U' < J$, independent of the size of the intraorbital Hubbard U.

We make no conclusion to the exact nature of the superconductivity in FeSe, instead concluding the existence of a pairing hierarchy. This hierarchy is dominated by intraband pairing, which leads to full gap [6,7,16,18] and back-bending [7], and where a small interband spin-orbit coupling mixes in interband pairing, which in turn leads to a two-peak tunneling spectrum [6,18] as a subleading phenomenon.

ACKNOWLEDGMENTS

We thank J. Kang, A. V. Chubukov, I. I. Mazin, A. Coldea, and R. Fernandes for discussion and input, and a special thanks to M. Watson for his correspondence. O.V. was supported by NSF Grant No. DMR-1506756.

APPENDIX A: GAP MINIMA WITHOUT SPIN-ORBIT COUPLING

ARPES experiment Ref. [7] reported no visible Fermi surface avoidance within ~5 meV resolution. This in turn constrains any interband spin-orbit coupling, which would mix the electronlike bands and avoid the Fermi surfaces (see Fig. 5). At the same time, STM on the same material (monolayer on $SrTiO_3$) shows the presence of two features, at energies 9 meV and 20.1 meV [18], with the high energy feature occurring far above the reported gap maximum in Ref. [7] (which is less than 14 meV, including uncertainty). In Sec. IV we discussed how

this, as well as the back-bending [7], implies the existence of a hierarchy, dominated by intraband pairing along independent electron pockets, and where the second STM feature occurs as a subleading phenomenon supported by interband pairing. We argued that without an interband spin-orbit coupling, there exists no pairing symmetry that opens a gap both at the Fermi level and above/below, which is necessary to produce the two STM features; however, with a small interband spin-orbit coupling (constrained to the resolution of the experiment [7]), the SU(2) spin symmetry is broken, contributing interband pairing to the dominant intraband pairing states.

There is, in fact, another piece of evidence for a small subleading contribution from interband pairing. The anisotropy of the superconducting gap in the monolayer as measured by ARPES [7] reports a gap minimum above the original normal state Fermi surface, with the smallest value of the gap occurring above the original Fermi surface crossing. Without interband pairing, the electron pockets are independent, and the direction of the crossing constitutes *no special direction*. Why then would the global gap minimum be found there? In fact, without interband spin orbit coupling to mix the electron pockets, no global gap minimum (or maximum) will generically occur in that direction. We show that here by a general analysis of pairing in the absence of interband spin-orbit coupling, i.e., $\lambda = 0$.

To begin, recognize first that, with $\lambda = 0$, the two electron pockets are independent. Thus, because they are related by symmetry, it is sufficient to focus on one electronlike pocket. We choose the X pocket and define the spin-generalized Nambu spinor $\Psi(k) = (\psi_{X,\alpha}(\mathbf{k}), \psi^\dagger_{X,\beta}(-\mathbf{k}))^T$, where $\alpha,\beta \in \{\uparrow,\downarrow\}$. The pairing Hamiltonian is then written as Eq. (A1):

$$H_{BdG} = \sum_{\mathbf{k}} \Psi(\mathbf{k})^\dagger \begin{pmatrix} h'^{\alpha}_X(\mathbf{k}) & \hat{\Delta}^\dagger_X \\ \hat{\Delta}_X & -h'^{\beta}_X(-\mathbf{k})^T \end{pmatrix} \Psi(\mathbf{k}). \quad \text{(A1)}$$

The pairing matrix $\hat{\Delta}_X$ is a 2×2 constant matrix; the exact contents of which are fixed by a particular choice of intraband pairing symmetry in Table III. For example, the s-wave (A_{1g}) pairing state is of the form Eq. (15). We write a generalized pairing matrix as Eq. (A2), where a,b,c,d are constants,

$$\hat{\Delta}_X = \begin{pmatrix} a & c \\ d & b \end{pmatrix}. \quad \text{(A2)}$$

Further, notice in Table III that there exists no intraband pairing symmetry that has both diagonal elements of $\hat{\Delta}_X$ and off-diagonal elements of $\hat{\Delta}_X$. This distinction is due to a difference in symmetry between those states of type intra-representational $1\otimes 1$ and $3\otimes 3$, and inter-representational $1\otimes 3$. This produces two possible scenarios: either (i) $a,b \neq 0$ with $c,d = 0$ or (ii) $c,d \neq 0$ with $a,b = 0$.

The 2×2 band Hamiltonian h'^{α}_X has two eigenstates, one downward dispersing and one that crosses the Fermi level. We are only interested in the geometry of the gap, which depends on those bands that cross the Fermi level. Projecting onto this reduced band basis simplifies H_{BdG} to a 2×2 matrix, which we define $\mathcal{H}$,

$$\mathcal{H}(\mathbf{k}) = \begin{pmatrix} \epsilon_X(\mathbf{k}) & \Delta^*_X(\mathbf{k}) \\ \Delta_X(\mathbf{k}) & -\epsilon_X(\mathbf{k}) \end{pmatrix}. \quad \text{(A3)}$$

We are interested in the form of the projected pairing function $\Delta_X(\mathbf{k})$, which inherited its momentum dependence from the band basis; defined in Bloch coordinates,

$$\Delta_X(\theta,\phi) = \langle X,\beta(\theta,\pi-\phi)|\hat{\Delta}_X|X,\alpha(\theta,\phi)\rangle. \quad \text{(A4)}$$

We now discuss Eq. (A4) for all (i) intra- and (ii) inter-representational pairing symmetries, respectively. We show that the gap anisotropy of (i) takes the form $|\cos\theta|$ and (ii) takes the form of $|\sin\theta|$, neither of which are generically maximum or minimum in the direction of the Fermi surface crossings.

1. Intrarepresentational; $a,b \neq 0$, $c,d = 0$

There are two intraband intrarepresentational symmetries in Table III: A_{1g} and B_{2g}. Both are spin singlets and thus both can be represented by the Nambu spinor $\Psi(\mathbf{k}) = (\psi_{X\uparrow}(\mathbf{k}), \psi_{X\downarrow}(-\mathbf{k}))^T$. The pairing function for these states takes the form of Eq. (A5):

$$\begin{aligned}\Delta_X(\theta,\phi) &= \langle X,\uparrow(\theta,\phi)|\hat{\Delta}_X|X,\uparrow(\theta,\phi)\rangle \\ &= \frac{a+b}{2} + \frac{a-b}{2}\cos\theta. \end{aligned} \quad \text{(A5)}$$

For a,b such that Δ_X is not nodal, the critical point of gap $|\Delta_X|$ occurs where $|\cos\theta|$ is largest.

2. Interrepresentational; $c,d \neq 0$, $a,b = 0$

There are two intraband inter-representational symmetries in Table III: E_u and $E_u\times \mathrm{U}(1)$. The E_u pairing state is nodal. The $E_u\times\mathrm{U}(1)$ (helical p-wave) pairing state is a spin triplet and, for understanding the gap geometry (see Sec. VII), is sufficiently represented by the Nambu spinor $\Psi(\mathbf{k}) = (\psi_{X\uparrow}(\mathbf{k}), \psi^\dagger_{X\uparrow}(-\mathbf{k}))^T$. The fully gapped pairing function takes the form of Eq. (A6):

$$\begin{aligned}\Delta_X(\theta,\phi) &= \langle X,\downarrow(\theta,\phi)|\hat{\Delta}_X|X,\uparrow(\theta,\phi)\rangle \\ &= -(c+d)\cos\frac{\theta}{2}\sin\frac{\theta}{2}e^{-i\phi} \\ &= -\frac{c+d}{2}\sin\theta\, e^{-i\phi}. \end{aligned} \quad \text{(A6)}$$

Thus the maximum/minimum in the gap $|\Delta_X|$ depends on the maximum/minimum of $|\sin\theta|$.

APPENDIX B: SYMMETRY GENERATORS AND TABLE OF IRREDUCIBLE REPRESENTATIONS

A complete study of the space group symmetry of iron-based superconductors [19] was worked out by Cvetkovic and one of us. In order to assist the reader, we list here all irreducible representations at the Γ point and those representations at the M point essential to this paper (i.e., $M1$ and $M3$). There are three generators of symmetry (see Fig. 1): two mirrors followed by a fractional translation $m_X t$ and $m_z t$ and one mirror m_x. With respect to representations of the group $\mathbf{P}_\Gamma$, it is sufficient to consider all three mirrors without fractional translations: m_X, m_z, and m_x. This is because $\mathbf{P}_\Gamma$ is isomorphic to $\mathbf{D_{4h}}$ [19]. (See Tables VI and VII.)

TABLE VI. Irreducible representations of group $\mathbf{P}_\Gamma$ [19].

$\mathbf{P}_\Gamma$	$m_X t$	$m_z t$	m_x
$A_{1g/u}$	± 1	± 1	± 1
$A_{2g/u}$	∓ 1	± 1	∓ 1
$B_{1g/u}$	∓ 1	± 1	± 1
$B_{2g/u}$	± 1	± 1	∓ 1
$E_{g/u}$	$\begin{pmatrix} \pm 1 & 0 \\ 0 & \mp 1 \end{pmatrix}$	$\begin{pmatrix} \mp 1 & 0 \\ 0 & \mp 1 \end{pmatrix}$	$\begin{pmatrix} 0 & \mp 1 \\ \mp 1 & 0 \end{pmatrix}$

TABLE VII. Irreducible representations $M1$ and $M3$ of group $\mathbf{P}_\mathbf{M}$ [19].

$\mathbf{P}_\mathbf{M}$	$m_X t$	$m_z t$	m_x
$M1$	$\begin{pmatrix} -1 & 0 \\ 0 & -1 \end{pmatrix}$	$\begin{pmatrix} -1 & 0 \\ 0 & 1 \end{pmatrix}$	$\begin{pmatrix} 0 & 1 \\ 1 & 0 \end{pmatrix}$
$M3$	$\begin{pmatrix} 1 & 0 \\ 0 & -1 \end{pmatrix}$	$\begin{pmatrix} -1 & 0 \\ 0 & 1 \end{pmatrix}$	$\begin{pmatrix} 0 & 1 \\ 1 & 0 \end{pmatrix}$

[1] G. R. Stewart, Superconductivity in iron compounds, Rev. Mod. Phys. **83**, 1589 (2011).

[2] D. Huang and Jennifer E. Hoffman, Monolayer FeSe on $SrTiO_3$, Annu. Rev. Condens. Matter Phys. **8**, 311 (2017).

[3] Y. Kamihara *et al.*, Iron-based layered superconductor: LaOFeP, J. Am. Chem. Soc. **128**, 10012 (2006).

[4] Y. Kamihara *et al.*, Iron-based layered superconductor $La[O_{1-x}F_x]FeAs$ ($x = 0.05$–0.12) with $T_c = 26$ K, J. Am. Chem. Soc. **130**, 3296 (2008).

[5] S. Medvedev *et al.*, Electronic and magnetic phase diagram of β-$Fe_{1.01}Se$ with superconductivity at 36.7 K under pressure, Nat. Mater. **8**, 630 (2009).

[6] Z. Du *et al.*, Scrutinizing the double superconducting gaps and strong coupling pairing in $(Li_{1-x}Fe_x)$OHFeSe, Nat. Commun. **7**, 10565 (2016).

[7] Y. Zhang, J. J. Lee, R. G. Moore, W. Li, M. Yi, M. Hashimoto, D. H. Lu, T. P. Devereaux, D.-H. Lee, and Z.-X. Shen, Superconducting Gap Anisotropy in Monolayer FeSe Thin Film, Phys. Rev. Lett. **117**, 117001 (2016).

[8] J.-F. Ge *et al.*, Superconductivity above 100 K in single-layer FeSe films on doped $SrTiO_3$, Nat. Mater. **14**, 285 (2015).

[9] S. Kanayama, K. Nakayama, G. N. Phan, M. Kuno, K. Sugawara, T. Takahashi, and T. Sato, Two-dimensional Dirac semimetal phase in undoped one-monolayer FeSe film, Phys. Rev. B **96**, 220509(R) (2017).

[10] Q. Song *et al.*, Phonon-enhanced superconductivity at the FeSe/$SrTiO_3$ interface, arXiv:1710.07057.

[11] S. N. Rebec, T. Jia, C. Zhang, M. Hashimoto, D.-H. Lu, R.-G. Moore, and Z.-X. Shen, Coexistence of Replica Bands and Superconductivity in FeSe Monolayer Films, Phys. Rev. Lett. **118**, 067002 (2017).

[12] A. Fedorov *et al.*, Effect of nematic ordering on electronic structure of FeSe, Sci. Rep. **6**, 36834 (2016).

[13] M. D. Watson, T. K. Kim, L. C. Rhodes, M. Eschrig, M. Hoesch, A. A. Haghighirad, and A. I. Coldea, Evidence for unidirectional nematic bond ordering in FeSe, Phys. Rev. B **94**, 201107(R) (2016).

[14] M. D. Watson *et al.*, Electronic anisotropies revealed by detwinned angle-resolved photo-emission spectroscopy measurements of FeSe, New J. Phys. **19**, 103021 (2017).

[15] Z. Du *et al.*, Experimental demonstration of the sign reversal of the order parameter in $(Li_{1-x}Fe_x)OHFe_{1-y}Zn_ySe$, Nat. Phys. **14**, 134 (2018).

[16] X. H. Niu, R. Peng, H. C. Xu, Y. J. Yan, J. Jiang, D. F. Xu, T. L. Yu, Q. Song, Z. C. Huang, Y. X. Wang, B. P. Xie, X. F. Lu, N. Z. Wang, X. H. Chen, Z. Sun, and D. L. Feng, Surface electronic structure and isotropic superconducting gap in $(Li_{0.8}Fe_{0.2})$OHFeSe, Phys. Rev. B **92**, 060504 (2015).

[17] L. Zhao *et al.*, Common electronic origin of superconductivity in (Li, Fe)OHFeSe bulk superconductor and single-layer FeSe/$SrTiO_3$ films, Nat. Commun. **7**, 10608 (2016).

[18] Q. Y. Wang *et al.*, Interface-induced high-temperature superconductivity in single unit-cell FeSe films on $SrTiO_3$, Chin. Phys. Lett. **29**, 037402 (2012).

[19] V. Cvetkovic and O. Vafek, Space group symmetry, spin-orbit coupling, and the low-energy effective Hamiltonian for iron-based superconductors, Phys. Rev. B **88**, 134510 (2013).

[20] O. Vafek and A. V. Chubukov, Hund Interaction, Spin-Orbit Coupling and the Mechanism of Superconductivity in Strongly Hole-Doped Iron Pnictides, Phys. Rev. Lett. **118**, 087003 (2017).

[21] J. Kang and R. M. Fernandes, Superconductivity in FeSe Thin Films Driven by the Interplay Between Nematic Fluctuations and Spin-Orbit Coupling, Phys. Rev. Lett. **117**, 217003 (2016).

[22] D. F. Agterberg, T. Shishidou, J. O'Halloran, P. M. R. Brydon, and M. Weinert, Resilient Nodeless *d*-Wave Superconductivity in Monolayer FeSe, Phys. Rev. Lett. **119**, 267001 (2017).

[23] S. V. Borisenko *et al.*, Direct observation of spin-orbit coupling in iron-based superconductors, Nat. Phys. **12**, 311 (2016).

[24] Y. Wang and A. H. MacDonald, Mixed-state quasiparticle spectrum for *d*-wave superconductors, Phys. Rev. B **52**, R3876(R) (1995).

[25] A. V. Chubukov, O. Vafek, and R. M. Fernandes, Displacement and annihilation of Dirac gap nodes in *d*-wave iron-based superconductors, Phys. Rev. B **94**, 174518 (2016).

[26] E. M. Nica, R. Yu, and Q. Si, Orbital-selective pairing and superconductivity in iron selenides, npj Quantum Mater. **2**, 24 (2017).